chemosensors

MDPI

Review

Room Temperature Resistive Hydrogen Sensor for Early Safety Warning of Li-Ion Batteries

Sixun Li [1], Shiyu Zhou [2], Shuaiyin Zhao [3], Tengfei Jin [1], Maohua Zhong [3], Zhuhao Cen [1], Peirong Gao [1], Wenjun Yan [1,*] and Min Ling [2]

[1] School of Automation, Hangzhou Dianzi University, Hangzhou 310018, China
[2] Department of Chemical and Biological Engineering, Zhejiang University, Hangzhou 310027, China
[3] HDU-ITMO Joint Institute, Hangzhou Dianzi University, Hangzhou 310018, China
* Correspondence: yanwenjun@hdu.edu.cn

Abstract: Lithium-ion batteries (LIBs) have become one of the most competitive energy storage technologies. However, the "thermal runaway" of LIBs leads to serious safety issues. Early safety warning of LIBs is a prerequisite for the widely applications of power battery and large-scale energy storage systems. As reported, hydrogen (H_2) could be generated due to the reaction of lithium metal and polymers inside the battery. The generation of H_2 is some time earlier than the "thermal runaway". Therefore, the rapid detection of trace hydrogen is the most effective method for early safety warning of LIBs. Resistive hydrogen sensors have attracted attention in recent years. In addition, they could be placed inside the LIB package for the initial hydrogen detection. Here, we overview the recent key advances of resistive room temperature (RT) H_2 sensors, and explore possible applications inside LIB. We explored the underlying sensing mechanisms for each type of H_2 sensor. Additionally, we highlight the approaches to develop the H_2 sensors in large scale. Finally, the present review presents a brief conclusion and perspectives about the resistive RT H_2 sensors for early safety warning of LIBs.

Keywords: resistive; hydrogen sensor; room temperature; early safety warning; Li-ion batteries

Citation: Li, S.; Zhou, S.; Zhao, S.; Jin, T.; Zhong, M.; Cen, Z.; Gao, P.; Yan, W.; Ling, M. Room Temperature Resistive Hydrogen Sensor for Early Safety Warning of Li-Ion Batteries. *Chemosensors* **2023**, *11*, 344. https://doi.org/10.3390/chemosensors11060344

Academic Editor: Francisco Márquez

Received: 4 May 2023
Revised: 8 June 2023
Accepted: 10 June 2023
Published: 12 June 2023

1. Introduction

In recent years, rechargeable lithium-ion batteries (LIBs) have become one of the most competitive energy storage technologies in the fields of portable electronic devices including cell phones and laptops, electric vehicles, and even large-scale energy storage (Figure 1a) due to their eco-friendliness and efficient storage of energy [1–5]. LIBs are usually sealed in stainless-steel, an aluminum or plastic package, consisting of Li-metal-oxide cathode and graphite anode, a polymer separator, and liquid electrolyte. The liquid electrolyte containing lithium salt and organic solvent is conductive, which connects the cathode and anode. Meanwhile, the polymer separator prevents short-circuiting of the cathode and anode. Li ions transport through the electrolyte causing the battery to recharge and re-discharge, as shown in Figure 1b [1].

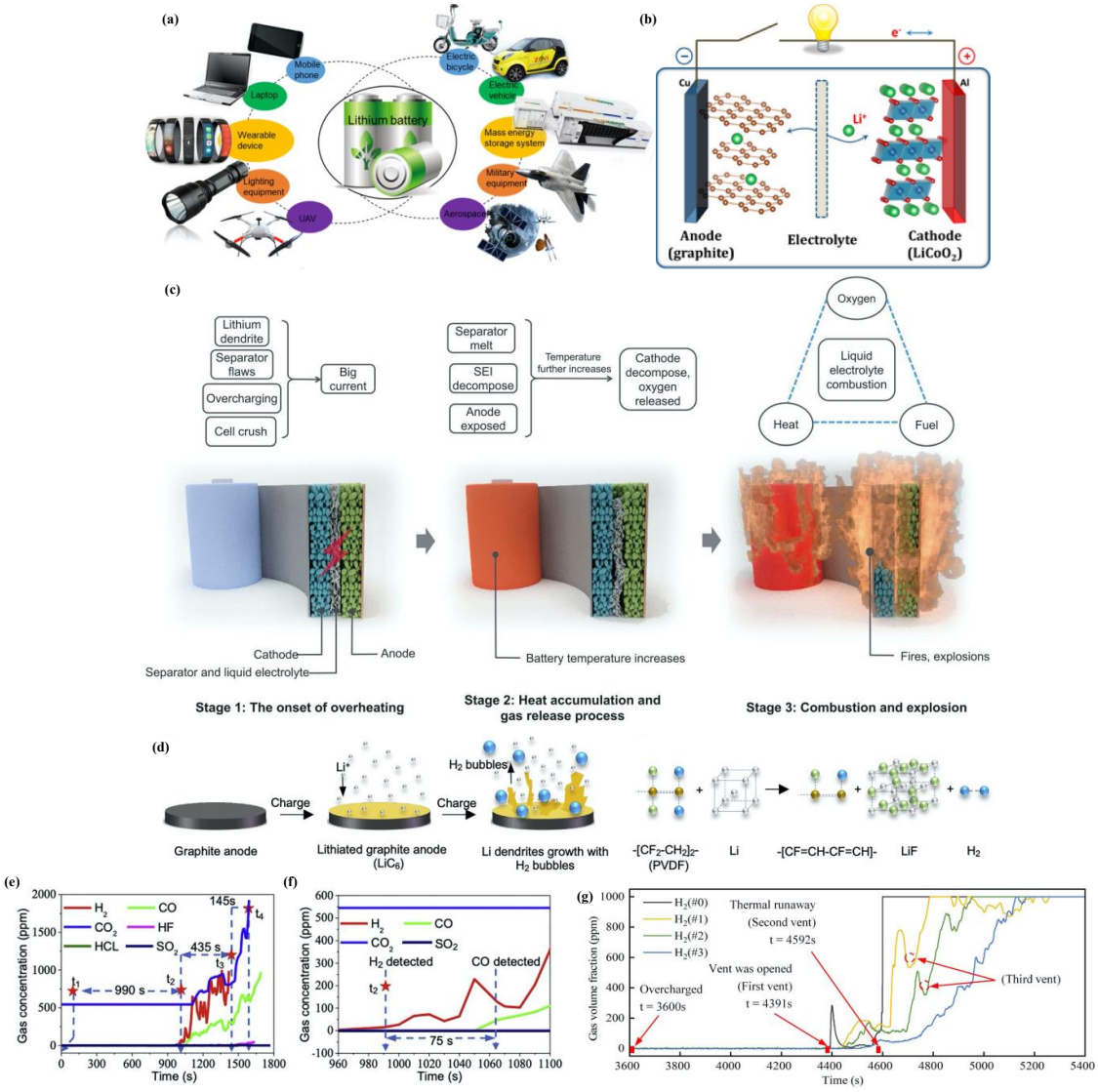

Figure 1. (**a**) Various applications of LIBs [5]. Copyright 2021 with permission from Elsevier. (**b**) Schematic illustration of Li-ion battery ($LiCoO_2$/Li^+ electrolyte/graphite) [1]. Copyright © 2013 American Chemical Society. (**c**) "Thermal runaway" process of LIBs [6]. Copyright © 2018 Science, open access. (**d**) Illustration of the mechanism of H_2 gas generation in LIB [7]. Overcharge experiment of a $LiFePO_4$ battery pack (8.8 kWh) with online detection of H_2, CO, CO_2, HF, HCl and SO_2: (**e**) gas concentration variation in 0–1800 s, (**f**) enlarged gas concentration curves in 960–1100 s [7]. Copyright 2020 with permission from Elsevier. (**g**) Gas concentration detected by H_2 detectors in LIBs energy-storage cabin during overcharge experiment [8]. Copyright 2023 with permission from Elsevier.

However, "thermal runaway" of LIBs frequently occurs due to Li dendrite unavoidably growth on graphite anodes under fast or long cycling situations, which is usually accompanied by toxic and flammable gases generation causing serious safety incidents such as fire and explosion (Figure 1c) [6,7,9]. The new regulations of "Safety Requirements for Power Batteries for Electric Vehicles" and "Global Technical Regulations for Safety of Electric Vehicles" require timely warning at least five minutes before serious incidents. In megawatt power grid energy storage of LIBs, security challenges are more serious. Therefore, early safety warning of LIBs is a prerequisite for the widely applications of energy storage systems based on LIBs.

The present safety warning system of LIBs is based on a battery energy storage system, chiefly relying on the protection of battery manage system (BMS), smoke detection, and some special gases detection [10,11]. The current BMS protect a battery by detecting its external surface temperature, voltage, and state of charge. For the special gases (such as hydrocarbons and CO) and smoke detection, they come from the reduction and oxidation of electrolytes at high temperature after "thermal runaway" is occurring [12–16]. Therefore, a more timely and reliable detection method before "thermal runaway" occurs is urgently need.

Recently, some research studies concerning early warning of battery failure based on venting gas signal have been reported [7,8,17,18]. Especially, Jin and Cui et al. [7] reported that H_2 detection could be an efficient safety indicator during the Li dendrite growth period before "thermal runaway" due to the H_2 produced by the reaction of Li dendrite and common electrode polymer binders (i.e., polyvinylidene fluoride (PVDF)) (Figure 1d). When the gas accumulation inside a battery cell reaches a high level, the battery vent ruptures and the gases are leased. Furthermore, H_2 was first detected among released gases (H_2, CO, CO_2, HCl, HF, and SO_2) from the battery and much earlier (over 10 minutes) than the rapid temperature increasing and smoke and fire detection (Figure 1e,f)) [7]. Obviously, H_2 detection inside lithium-ion battery cell is the most effective measure for the early safety warning of LIBs. However, the research on H_2 detection inside battery cells is still in an early stage; literatures covering the relevant experimental research are very limited. Jin et al. [8] further investigated H_2 gas diffusion behavior and the H_2 detector installation of LIBs energy-storage cabin. The H_2 detectors in the cabin could warn about 116 s before thermal runaway, as they set a consistent warning value of 20 ppm for H_2 (Figure 1g).

Various H_2 gas sensors have been studied in the last few decades, such as FET [19–21], Schottky barrier [22–25], Capacitive [26], surface acoustic wave [27–29], and resistive [30–32]. Among them, resistive H_2 sensors are operated by the transduction of chemical reactions into resistance signals, offering some benefits of low detection limit (LOD) at the ppb level for flexible and simple devices, and could potential work at room temperature. Therefore, they are the most promising for the early safety warning of LIBs [33]. The operation of resistive H_2 sensors rely on the reactions between H_2 and sensing materials. Palladium (Pd)-based H_2 sensors are the current state-of-the-art resistive H_2 sensors, including Pd-based bimetals, and Pd-based composites [31,34–37]. In addition, homogeneous and heterogeneous designs based on other metals, metal oxide (MOXs), carbon nanotubes (CNTs), graphene, and transition dichalcogenides (TMDs) are studied for efficient H_2 sensing [38]. Although resistive hydrogen sensors have dramatically advanced in recent years, to the best of our knowledge, resistive H_2 sensors integrated inside of LIB cells has not been reported yet.

Due to the harsh application condition of H_2 sensor inside of LIB cell, special requirements are put forward. For examples, high temperature is dangerous for LIBs, so the internal H_2 sensor should operate without heater; for efficient and valid warning, the detection concentration of internal H_2 sensor is suggested to be higher than 20 ppm according to previous reports, with response time of less than 116 s [7,8]; owing to the detection under electrolyte vapors, the internal H_2 sensor needs great selectivity. Therefore, there remain huge challenges for the internal H_2 sensors applied for the early safety warning of LIBs, especially in terms of the accuracy, selectivity, long-term stability, and compatibility while operating at room temperature under harsh environment inside of LIB cell.

In this review, we present a comprehensive overview of the recent advances and underlying mechanisms in resistive H_2 sensors, which are possible to work inside of LIB cell, from three aspects: (1) operating at room temperature, (2) selectivity, and (3) internal gas sensors in LIB. We highlight the recent key advances and strategies for the realization of H_2 sensors in the applications of LIBs. H_2 sensors based on various materials are discussed, as well as the key H_2 sensing mechanisms. Then, we discuss the challenges and prospects of resistive H_2 sensors for the early safety warning of LIBs. We hope that this review could

provide and stimulate valuable ideas for the evolution of H_2 sensors in LIBs systems, as well as and propel the development of LIBs.

2. Resistive H_2 Sensor Operating at Room Temperature

For LIBs, a high internal temperature probably induces additional violent exothermic chemical reactions for further heat generation, resulting in thermal runaway of LIBs. Hence, room temperature H_2 sensors applied inside of LIB is necessary. Resistive H_2 sensors operating at room temperature mainly rely on the catalytic adsorption of H_2 molecule on noble metal (for example Pd, Au, Pt). Among of them, Pd-based H_2 sensors are the current state-of-the-art resistive H_2 sensors. Beyond that, synergistic effect of heterojunctions, metallization effect of special metal oxide [39,40], and efficient H_2 sensing capacity of emerging materials (i.e., MXene, TMDs) at low temperatures have also been investigated to develop RT H_2 sensor.

2.1. Pd-Based H_2 Sensors

Basic H_2 Sensing Mechanism

Generally, the H_2 sensing mechanism of Pd-based H_2 sensors are catalytic adsorption of H_2 on Pd, which induces the dissociation of H_2 molecule into H atoms and the formation of PdH_x (Equations (1) and (2)) [31,41].

$$H_2(gas) \rightarrow H_2(ads) \quad (1)$$

$$Pd + \frac{x}{2}H_2(ads) \rightarrow PdH_x \quad (2)$$

Numerous resistive Pd-based H_2 sensors have been developed, including pure Pd nanostructures and Pd-based composites, such as Pd-hetero metal, Pd-MOX, Pd-carbon material, and Pd-TMD. In this section, we discuss the sensing mechanisms, effect factors and key advances in recent several years of the resistive H_2 sensors based on Pd and Pd composites.

Pure Pd materials. According to Equations (1) and (2), PdH_x is formed when H_2 molecules adsorb on Pd surface. Conductivity of PdH_x is poorer than Pd, which generates H_2 response in resistance of Pd [31,42]. Plenty of resistive H_2 sensors based on pure Pd materials have been reported. With the significant development of nanoscience, various Pd nanostructures with further H_2 sensing mechanisms were developed to enhance the H_2 sensing capacities [43–46].

Kim et al. [43] and Jung et al. [44] investigated the nanograin effects and the α-to-β phase transition of Pd on H_2 sensing. When the Pd crystallites < 10 nm, abundant nanogaps were created between the nanograins (<2 nm). The nanogaps between Pd nanograins intrinsically stem the electrical conduction. Exposed to different concentration of H_2, different kinds of conducting pathways were formed in Pd, yielding switchable H_2 sensing behaviors (Figure 2a,b) [44]. Similar phenomena were demonstrated in Ref. [31] (Figure 2c–g): (i) when exposed to low concentrations of H_2 (2.5 to 100 ppm), α-PdH_x was formed expanding Pd nanograins, which closed the narrow nanogaps and further producing a new conduction pathway. Obvious negative resistance response was observed. (ii) Upon exposed to moderate concentrations of H_2 (250 to 2500 ppm), most of the nanogaps were closed, resulting in saturation of the negative resistance response. (iii) Upon exposed to high concentrations of H_2 (0.5 to 3%), all nanogaps were closed and β-PdH_x were formed, while surface electron scattering generated by β-PdH_x dominantly the electrical conductions, leading to significant positive resistance response. Consequently, ultrasmall grain size of Pd are critical for H_2 detection at low concentrations, α-to-β phase transition of Pd could detect a wide range of H_2 concentrations from sub-ppm to 4%. In addition, negative effect of oxygen on Pd-based H_2 sensing has been demonstrated in earlier literatures [47,48]. We will discuss the effect in a later section.

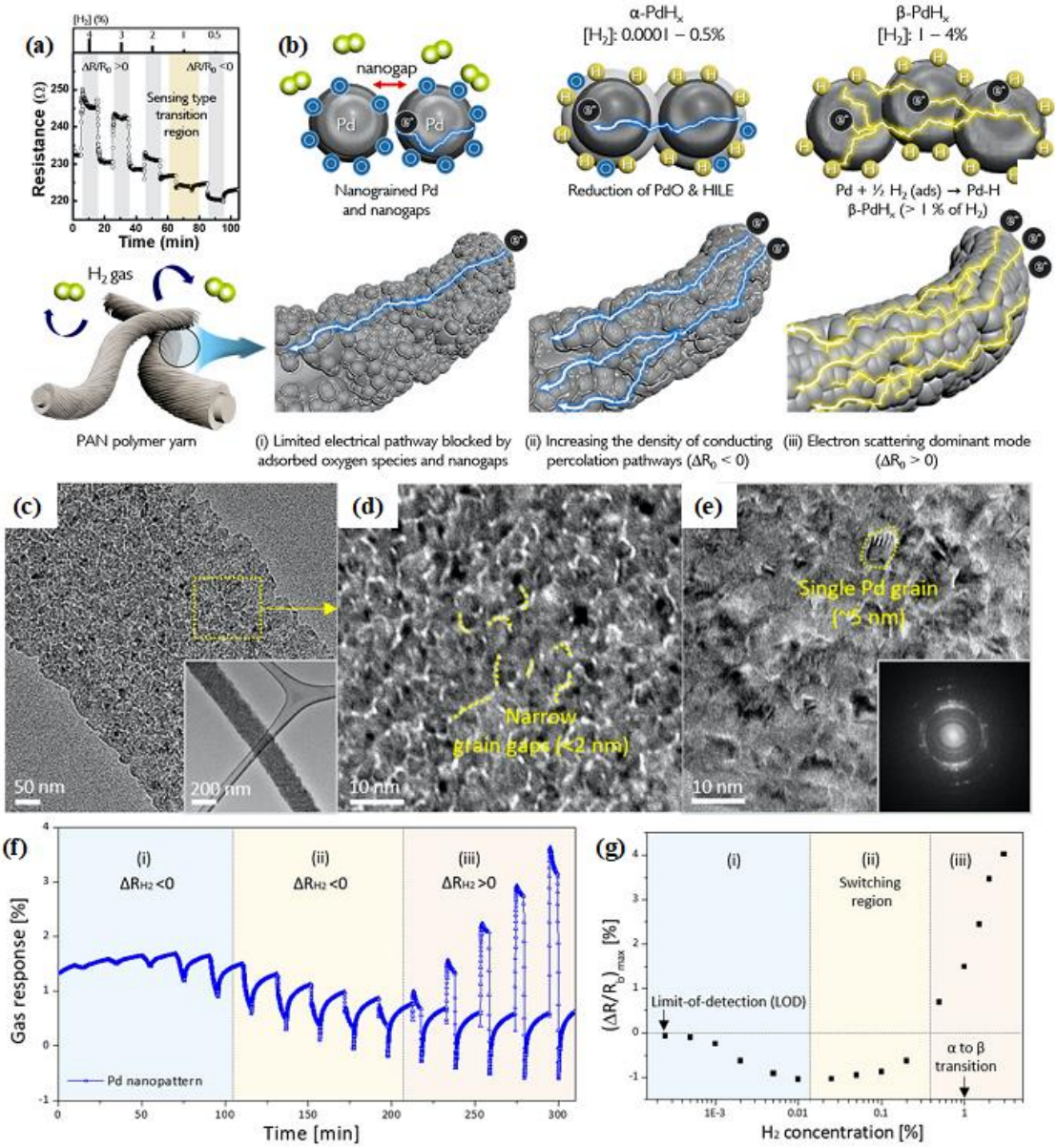

Figure 2. (**a**) Switchable H_2 sensing behavior of yarn@Pd sensor, and (**b**) the different kinds of conduction pathways in Pd under different concentrations of H_2 [43]. Copyright © 2019 American Chemical Society. (**c**–**e**) TEM images of ultrasmall grained Pd nanopattern, showing the nanogap of <2 nm and the Pd grain size of ~5 nm. (**f**) Real-time switching response and (**g**) the corresponding response amplitude with three distinct phases of Pd nanopattern sensor to various H_2 concentrations (2.5, 5, 10, 20, 50, 100, 250, 500, 1000, 2000, 5000, 10,000, 15,000, 20,000, 30,000 ppm). [44]. Copyright © 2018 American Chemical Society.

Pd-metal alloy. Recently, many researchers developed Pd-based alloys to improve the H_2 sensing properties, such as limit detection and response/recovery behavior [35,49–51]. Jung et al. [49] developed Pd/Pt and Pd/Au high surface-to-volume ratio nanopatterns (Figure 3a). Compared to Pd nanopattern, Pd/Pt nanopattern showed 45.5-fold higher response to 1% H_2 (Figure 3b,c), Pd/Au nanopattern showed about 73-fold and 4.6-fold enhancement in the response and recovery speed, respectively (Figure 3d–f). The dramatic improvements in response and recovery behaviors to H_2 are attributed to the ultrasmall size (<5 nm), ultrathin nanopattern (<15 nm), grain interfaces and the lower adsorption/dissociation energy of H_2 on Pd/Pt and Pd/Au surfaces (Figure 3g–j). Kim et al. [51]

developed hollow Pd-Sn alloy nanotubes with high surface area of 223.0 m^2/g for H_2 sensing and ultrafine grain size. Interestingly, the Pd-Sn alloy effectively prevented degradation of H_2 sensing performances caused by the α-β transition of Pd. As a result, the hollow Pd-Sn nanotubes exhibited outstanding sensing properties to a wide concentration range of H_2 (50 ppm to 3%), especially fast response/recovery rate to high concentration of H_2 (20 s/17 s to 2% H_2, Figure 4a–i). The noteworthy H_2 sensing mechanism was proposed: (i) The abundant interface gaps between the grains owing to larger atom size of Sn (0.141 nm) and smaller atom size of Pd (0.138 nm) dominated low concentration of H_2 (0.5 ppm to 0.02%) sensing behavior, due to the nanogap effect. (ii) For high concentration of H_2 (0.05% to 3%), the formation of β-PdH_x governed the H_2 sensing properties (Figure 4j). The H_2 sensing mechanism agreed with the previous reports [43,44].

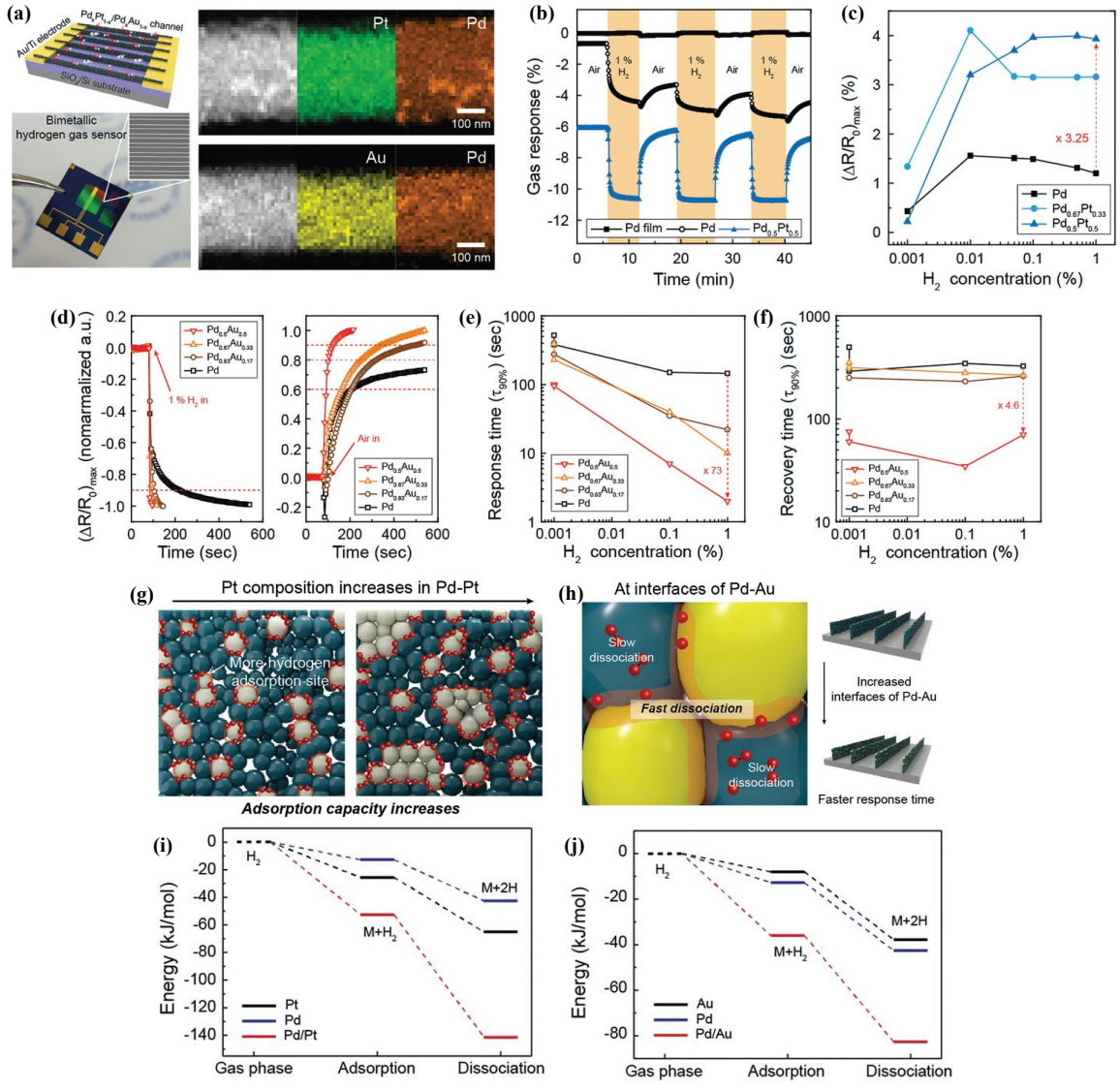

Figure 3. (**a**) Schematic illustration and photograph of the sensor device based on Pd/Pt (or Pd/Au), with the inset of SEM showing the nanopattern channel, and EDS mapping of Pd/Pt and Pd/Au sensing channels. Comparison of the H_2 sensing behaviors of Pd nanofilm, Pd nanopattern, and Pd/Pt nanopattern sensors: (**b**) real-time response and (**c**) response amplitude. Comparison of the H_2 sensing behaviors of Pd and Pd/Au nanopattern sensors: (**d**) response/recovery behavior, (**e**) response time, and (**f**) recovery time. H_2 sensing mechanism and the calculated adsorption/desorption energies of (**g**,**i**) Pd/Pt nanopattern, and (**h**,**j**) Pd/Au nanopattern [49]. Copyright 2019 with permission from Wiley.

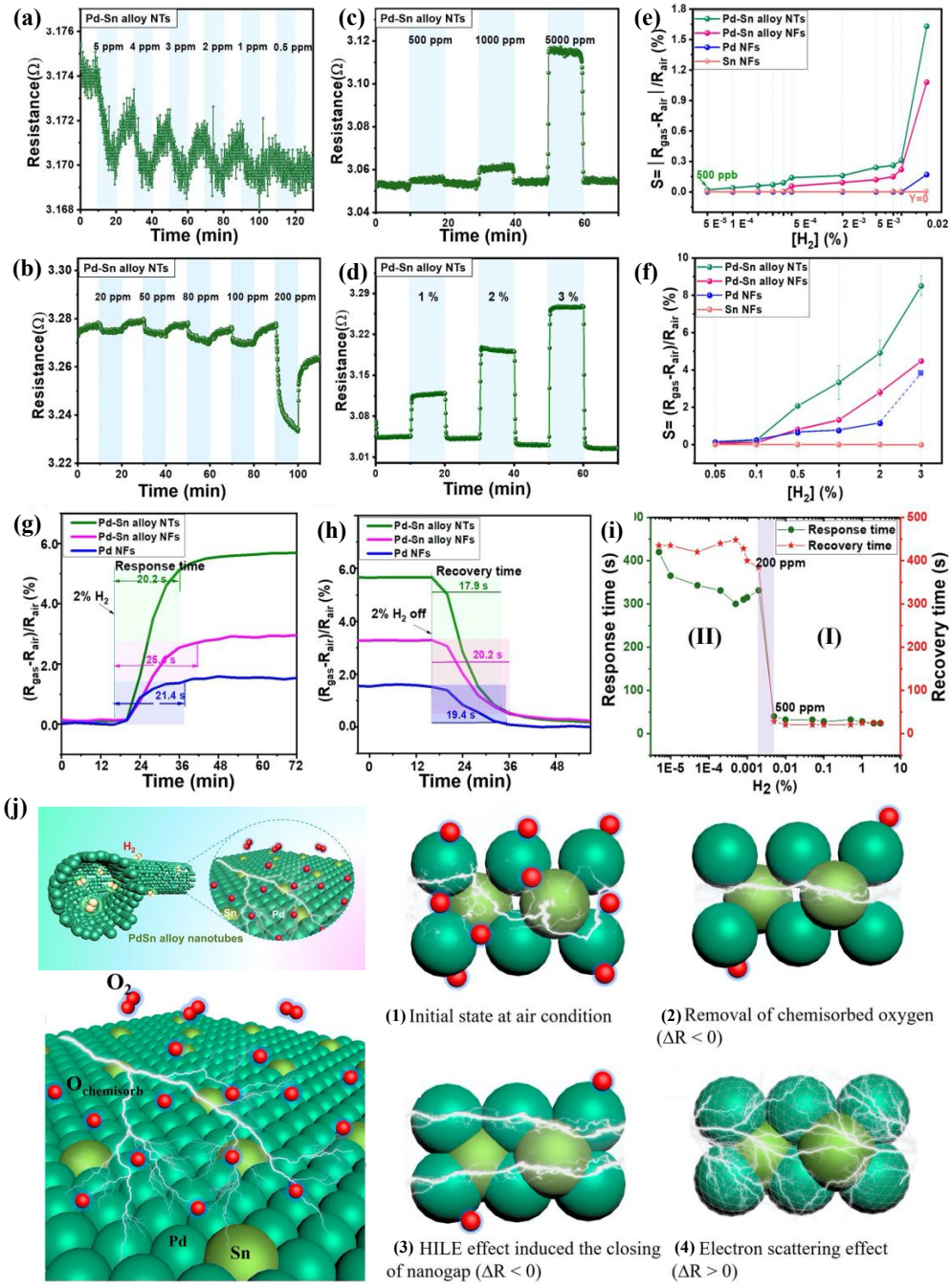

Figure 4. H_2 sensing performances of hollow Pd-Sn alloy nanotubes: (**a**–**d**) real-time response and (**e**,**f**) response amplitude to various concentration of H_2; (**g**) dynamic response and (**h**) dynamic recovery to 2% H_2; (**i**) response/recovery time vs. H_2 concentration. (**j**) Schematic illustration of H_2 sensing mechanism [51]. Copyright © 2022 American Chemical Society.

Pd-MOXs. MOXs are the classical gas sensing semiconductor materials. However, their H_2 sensing properties are limited at room temperature. Previously, many researchers developed Pd-MOX composites to achieve good H_2 sensing at room temperature. Here, we overview some interesting representative approaches of H_2 sensors based on Pd-MOX composites, reported recently.

Zhang et al. [46] investigated the interconvertible effect on H_2 sensing of catalyst nanoparticles and semiconductor support in Pd-decorated PdO hollow shells. They prepared PdO hollow shells, which were subsequently treated by $NaBH_4$ to be partially reduced into Pd on the PdO surface. The Pd nanoparticles were discretely and physically

inlaid on the surface of PdO with a ultrasmall size of ~ 2 nm (Figure 5a). The catalytic effect of Pd, as well as the Schottky-junction between Pd and PdO, enhanced the H_2 sensing performances even at 1 ppm (Figure 5b–d). Notably, inlaid Pd in PdO shells prevented the agglomeration of Pd nanoparticles, which generated long-term stability (Figure 5e).

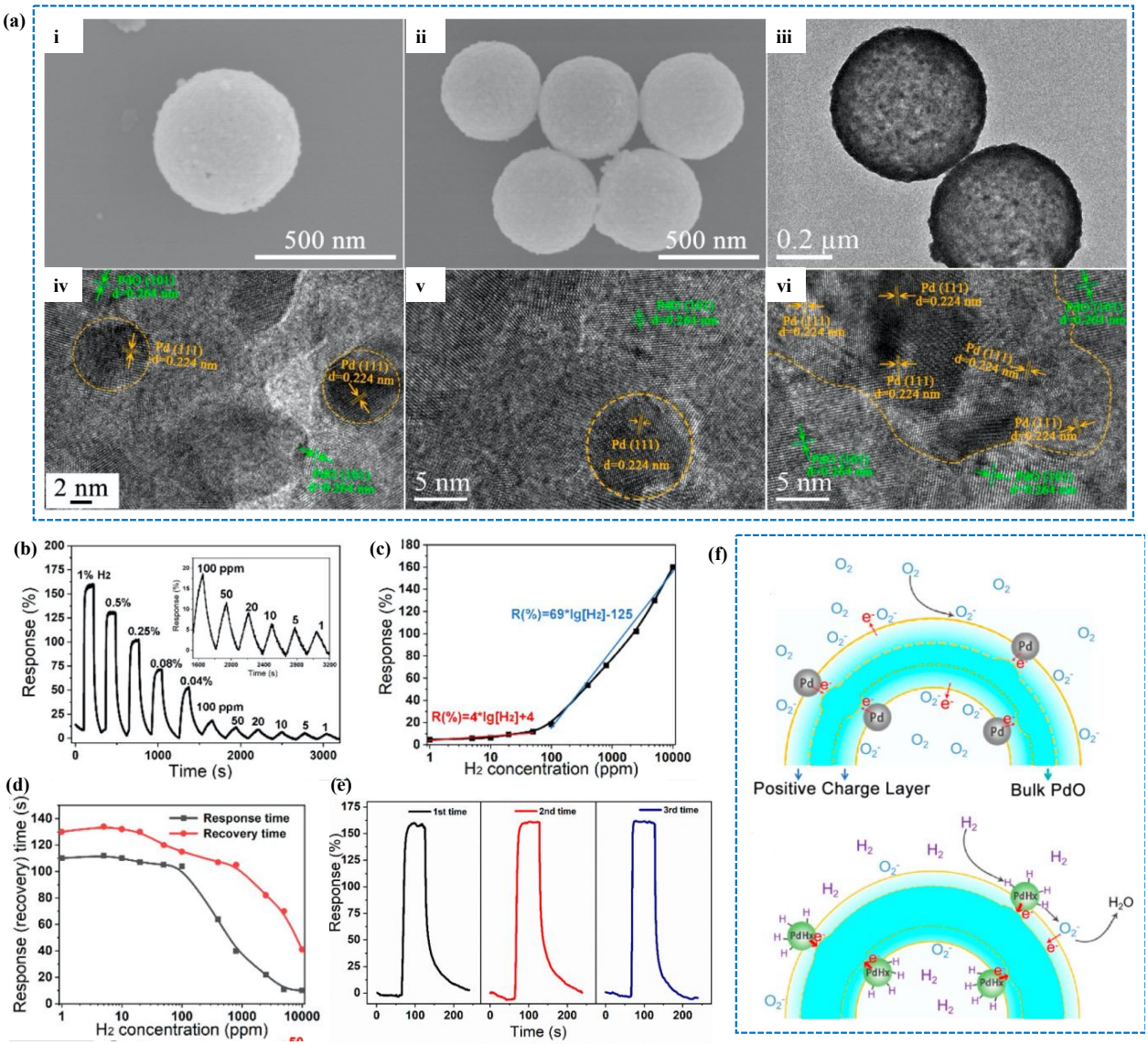

Figure 5. (**a**) Morphology of the $NaBH_4$-treated Pd-PdO hollow shells. H_2 sensing performances of the Pd-PdO hollow shells sensor: (**b**) real-time response; (**c**) plotted responses and (**d**) plotted response and recovery time with respect to H_2 concentration; (**e**) response to 1% H_2 reactivated for different periods. (**f**) H_2 sensing mechanism of Pd-PdO hollow shells [46]. Copyright 2020 American Chemical Society.

In addition, Zhang et al. [36] designed an unique conduction model by inserting a high-conductive metallic core Au into less-conductive p-type PdO to boost the RT H_2 sensing performances (Figure 6). As a result, Pd decorating Au@PdO demonstrated an ~90 times larger in H_2 response than Pd decorating Pd@PdO. And the boosted H_2 response helped the Pd-Au@PdO sensor showed ultralow LOD of 0.1 ppm. Pd-ZnO nanoflowers has been demonstrated RT H_2 sensing in ppb level with experimental LOD of 300 ppb, due to the change in channel conductance of ZnO nanoflowers based on the incorporation of Pd [37].

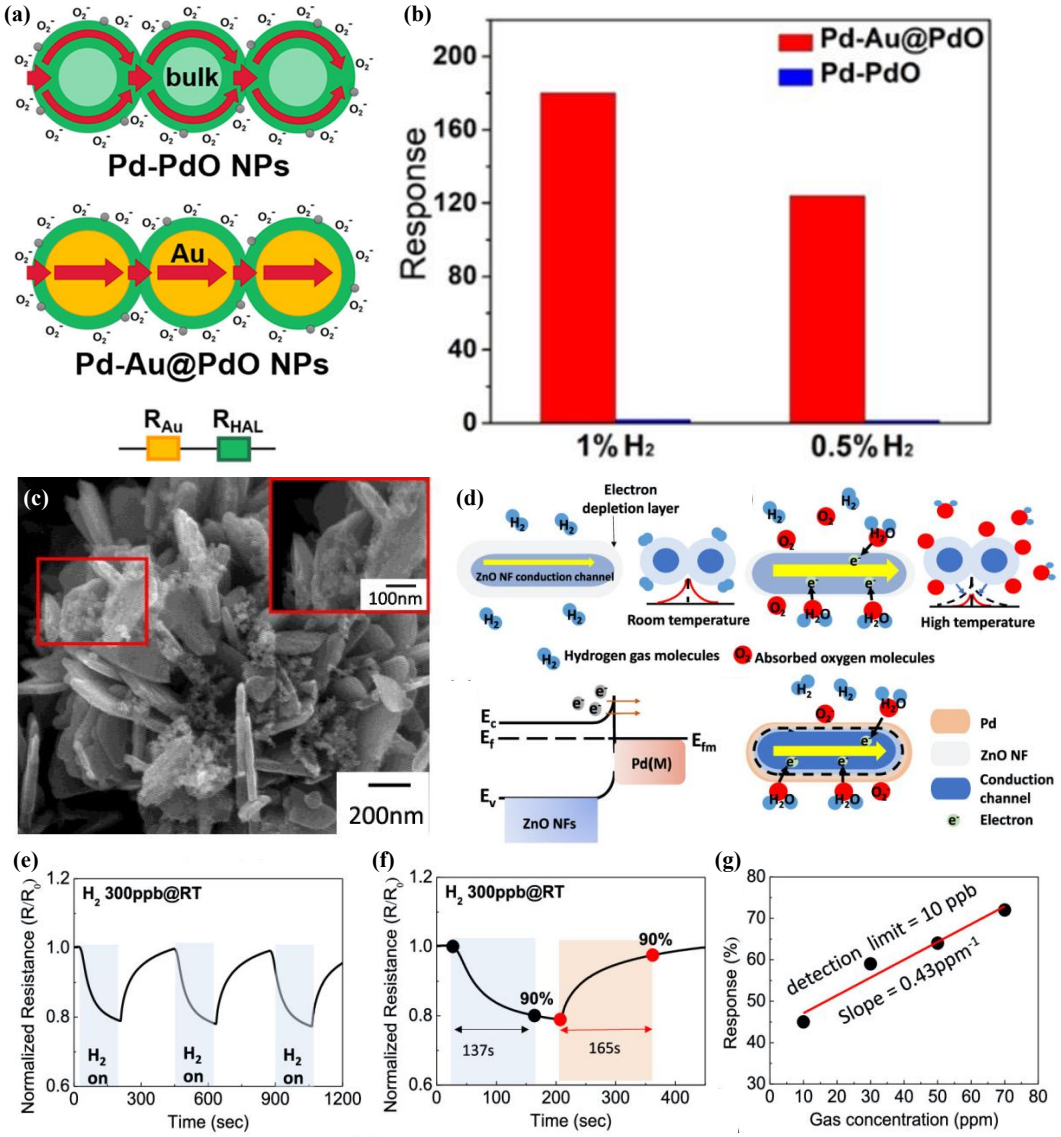

Figure 6. (**a**) Schematic illustration of gas sensing mechanism for Pd-PdO and Pd-Au@PdO. (**b**) Comparison of response to 1% H_2 and 0.5% H_2 for Pd-PdO and Pd-Au@PdO samples [36]. Copyright © 2021 American Chemical Society. (**c**) SEM and (**d**) H_2 sensing mechanism of Pd-ZnO nanoflowers. H_2 sensing performances at RT of Pd-ZnO nanoflowers sensor: (**e**) real-time response/recovery to 300 ppb H_2, (**f**) response/recovery time, and (**g**) response values vs. H_2 concentration. [37]. Copyright © 2021 American Chemical Society.

Pd-carbon materials. Carbon nanotubes, graphene, and their derivatives are very promising in the room temperature gas sensor fields, due to their good electrical conductivity at RT. However, H_2 molecule is very difficult to adsorb on the surface of carbon materials, due to weak H_2 adsorption capacity. In regard of this case, lots of Pd-carbon material composites have been previously investigated for RT H_2 sensors. Even so, low LOD and quick recovery behavior remain big challenges. As is well known, Pd particles at ultrasmall size are very helpful for the RT H_2 sensing. However, they are very easy to aggregate to further cause degradation of overall H_2 response.

For that, we designed Pd-graphene system via DNA assistant for trace of H_2 sensing [33]. During the synthesis process of one-pot solution method, DNA suppressed the stacking of graphene layers due to π-π interaction between DNA and graphene, meanwhile in-situ anchored PdO_2 subnanoscale clusters on the exfoliated single layer graphene

(Figure 7a,b). The design showed mimic wrinkled morphology and sensing mechanism of natural olfactory neuroepithelium, being named BONe (Figure 7a). The BONe boosted H_2 sensing performance (25 s/35 s at 5 ppm H_2 with experimental LOD of 50 ppb) at RT with yearlong durability (Figure 7c–e). High surface area of the BONe, good conductivity of graphene, as well as the subnanoscale of PdO_2, generated the ultra-sensitivity to ppb-level H_2 at RT; subnanoscale of PdO_2 anchored on graphene yielded yearlong stability. Notably, it was calculated that PdO_2 exhibited a d-band downshift of −2.58 eV, which was a much further downshift than that of PdO (−2.16 eV) and Pd (−0.179 eV), governing the complete and fast recovery behavior during H_2 detection (Figure 7f–h). A similar d-band theory was proposed previously, that tuning of d-band energy level balanced the adsorption and desorption capacities, and the lower the d-band level, the weaker the adsorption [52].

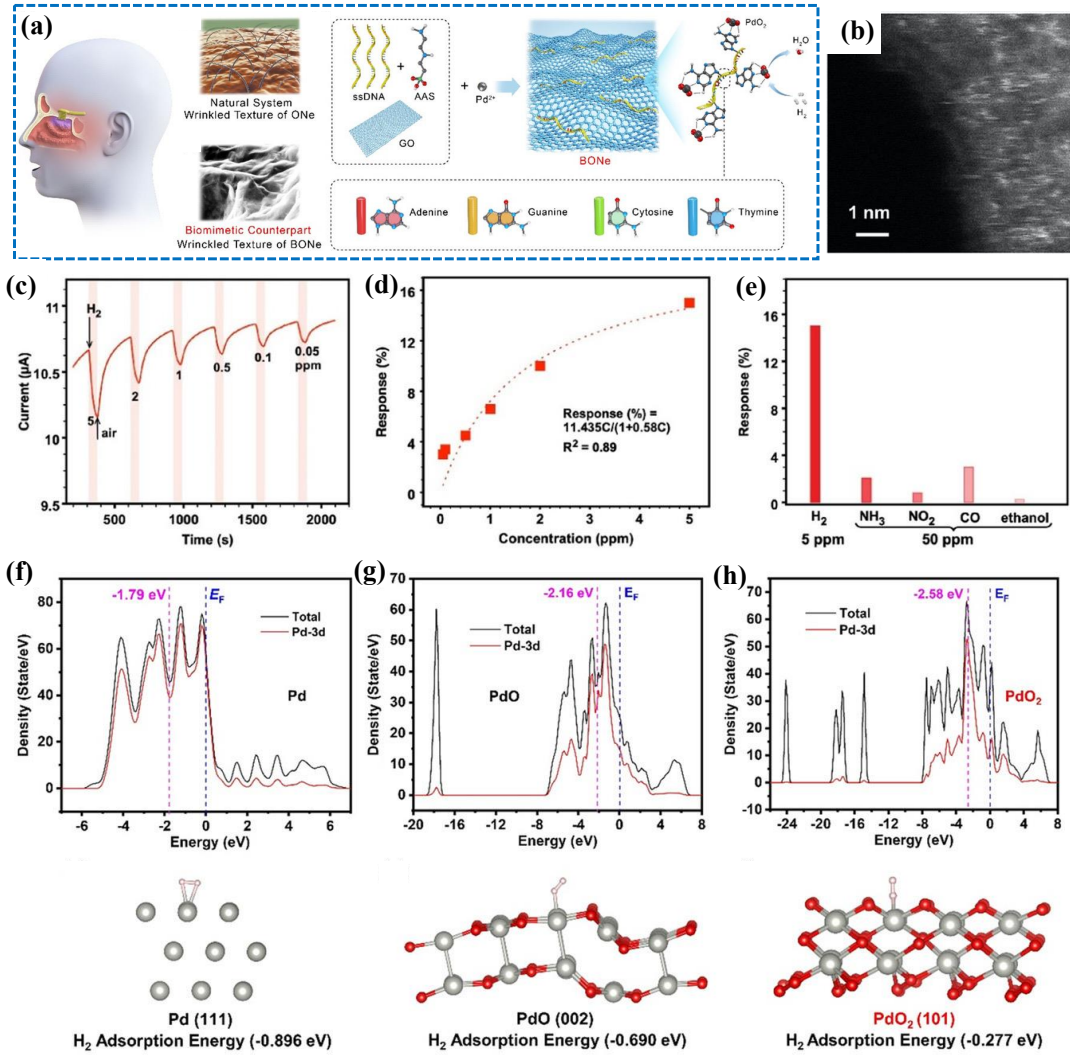

Figure 7. (**a**) Schematic diagram of the design and synthesis of BONe. (**b**) Cs-STEM-HAADF image of BONe showing subnano clusters of Pd. H_2 sensing performances of BONe at RT: (**c**) real-time response to various concentration of H_2, (**d**) response value vs. H_2 concentration, and (**e**) selectivity. D-band downshift calculation of (**f**) Pd, (**g**) PdO, and (**h**) PdO_2. [33]. Copyright 2023 Wiley, open access.

Pd-other materials. With the emerging of new materials (metal-organic frame MOF, Mxene, et al.), composites of Pd and kind of new materials were developed for H_2 sensing. The sensor based on flexible $Ti_3C_2T_x$ MXene@Pd nanoclusters, reported in Ref. [53] delivered a response/recovery time of 32/161 s and sensitivity of 23% to 4% H_2 at RT (Figure 8a–c). The strong H_2 adsorption into lattice of Pd nanoclusters induced electrons

doping in MXene, generating fast response behavior (Figure 8d). However, the limit of detection (0.5%) needs to be improved. The Pd-decorated sodium titanate nanoribbons (Pd-NTO NRs) developed by Zhang et al. [54] exhibited ultrafast response to 1% H_2 within 1.1 s at RT, and a wide detection range (0.8 ppm to 10% H_2). The excellent H_2 sensing capacity benefited from the laterally paralleled morphology and abundant oxygen vacancies on edge sites of nanoribbons, as well as monodispersed Pd nanoparticles in size of ~3.5 nm. Oxygen in air could block the reactive sites, leading to depress the H_2 sensitivity and retard the response/recovery rate [47,48]. For that, Kim and Penner et al. [55] designed patterned Pd nanowires covering ZIF-8 membrane (Pd NWs@ZIF-8) for H_2 sensing. Although the ZIF-8 membrane reduced the H_2 response slightly, 20-fold faster response/recovery rate (3.5% at 10/7 s to 1% H_2 versus 5.9% at 164/229 s of Pd nanowires) was achieved due to the molecular sieving and acceleration effects of ZIF-8 (Figure 8e) since the pore size of ZIF-8 is 0.34 nm, which is larger than the diffusion kinetic diameter of H_2 molecule (0.289 nm), but a little smaller than that of O_2 molecule (0.345 nm) (Figure 8e).

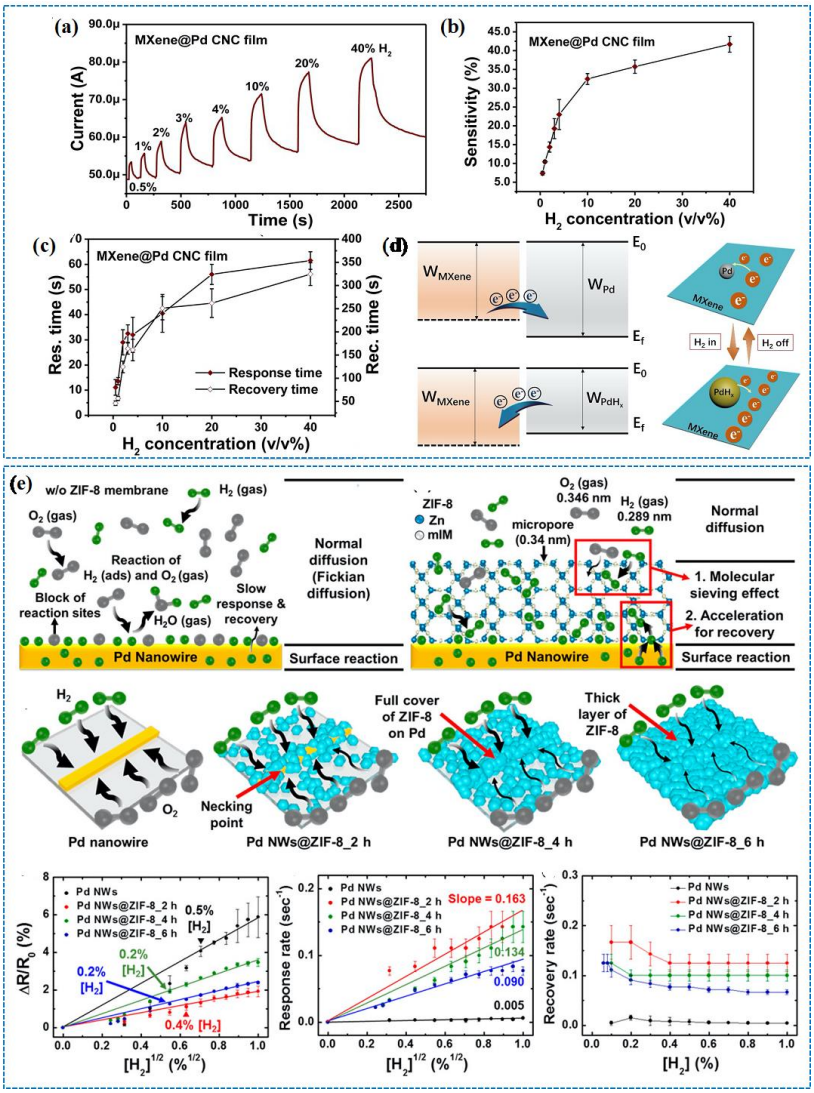

Figure 8. H_2 sensing performances of MXene@Pd: (**a**) real-time response to various concentration of H_2, (**b**) sensitivity and (**c**) response/recovery time vs. H_2 concentration. (**d**) H_2 sensing mechanism of MXene@Pd. [53] Copyright 2020 with permission from Elsevier. (**e**) H_2 sensing performances and mechanism of Pd NWs@ZIF-8. [55]. Copyright © 2017 American Chemical Society.

2.2. Other Noble Metal-Based H_2 Sensors

Similar to H_2 adsorption property of Pd, other noble metals also exhibit H_2 adsorption behavior [56]. Moreover, Au and Pt-based H_2 sensors has been demonstrated due to the formation of MH_x [57–59]. Guha et al. [57] reported Pt-functionalized rGO for excellent H_2 sensing at RT, 65 s/230 s against 5000 ppm H_2 with LOD of 200 ppm in air ambience. Interestingly, for this Pt-rGO composite, H_2 response was larger in N_2 environment than that in air ambience; however, sensor recovered faster in air than in N_2. In N_2 and air environments, H_2 first physisorbed on Pt-rGO surface and then dissociated to from Pt-H (Equation (3)). But in air, H_2 also reacted with the adsorbed oxygen on the Pt-rGO surface to form Pt-H and H_2O (Equations (4) and (5)).

$$Pt + \frac{1}{2}H_2 \rightarrow Pt - H \quad (3)$$

$$Pt + \frac{1}{2}O_2 \rightarrow Pt - O \quad (4)$$

$$Pt - O + \frac{3}{2}H_2 \rightarrow Pt - H + H_2O \quad (5)$$

The H_2O competed with H_2 molecules to adsorb on the Pt-rGO surface, reducing the H_2 response. On the contrary, the adsorbed H_2 and the dissociated H-atoms reacted with adsorbed oxygen to convert to water vapor while purging air, exhibiting fast recovery in air ambience. Similar effect of oxygen on Pd- and Pd@Pt-based H_2 sensing has been demonstrated in earlier literatures (Figure 9) [47,48].

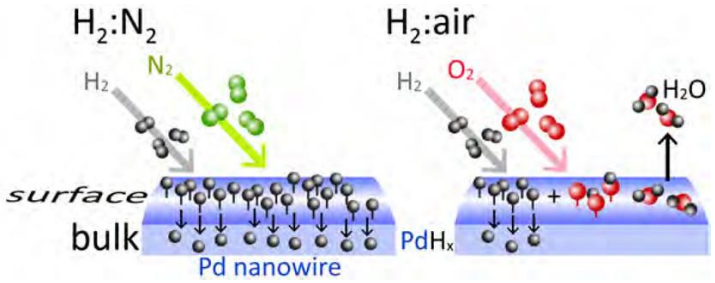

Figure 9. Schematic illustration of oxygen effect on Pd-based H_2 sensing. [47] Copyright 2015 American Chemical Society.

2.3. MOXs-Based H_2 Sensors

Generally, most MOXs-based resistive gas sensors operated at high temperature (>150 °C). However, recent approaches were developed to realize RT H_2 sensing performances of MOXs, such as nanostructure design [60–62], composites of MOXs [63,64], and surface metallization [37]. Huang et al. [61] demonstrated the well-aligned MoO_3 nanoribbon arrays exhibited great H_2 response/recovery behavior at RT, with a response/recovery time of 3 s/16 s at 100 ppm H_2 which is much shorter than 59 s/151 s of randomly arranged MoO_3 nanoribbons (Figure 10a–e). The accelerated H_2 response/recovery rate was due to the fact that the high alignment of nanoribbons could increase the surface activity of MoO_3 and suppress the nanojunction effect. On the contrary, in the randomly arranged MoO_3, the interface diffusion of adsorbed oxygen caused serious nanojunction effect, resulting in much slower H_2 response/recovery rate.

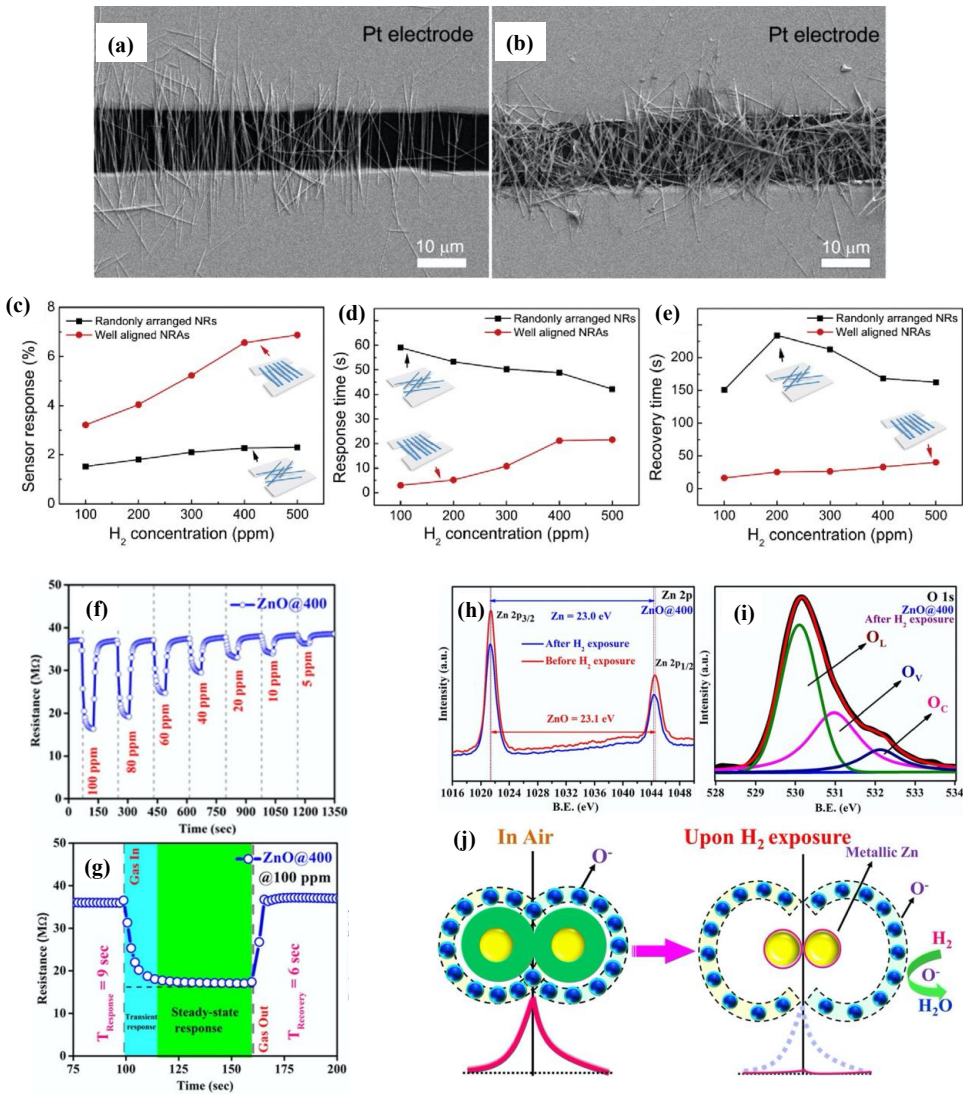

Figure 10. SEM images of (**a**) well-aligned MoO_3 nanoribbon arrays, and (**b**) randomly arranged MoO_3 nanoribbons. H_2 sensing properties of well-aligned MoO_3 nanoribbon arrays (NRAs) and randomly arranged MoO_3 nanoribbons (NRs): (**c**) sensor response, (**d**) response time, and (**e**) recovery time vs. H_2 concentration. [61] Copyright 2020 with permission from Elsevier. H_2 sensing performances of holey ZnO: (**f**) real-time resistance response to various concentration of H_2, and (**g**) response/recovery time to 100 ppm H_2. XPS spectra of (**h**) Zn 2p and (**i**) O 1 s in holey ZnO before and after H_2 exposure. (**j**) Schematic illustration of H_2 sensing mechanism of holey ZnO [39]. Copyright 2021 with permission from Elsevier.

Yun et al. [37] designed holey engineered 2D ZnO-nanosheets for supersensitive H_2 sensing (Figure 10f–j). The sensor exhibited 115% response to 100 ppm H_2 with short response/recovery time of 9 s/6 s at room temperature (Figure 10g). And the experimental LOD was 5 ppm (Figure 10f). Upon exposure to H_2, surface of the ZnO nanosheets became metallic Zn (Figure 10h,i). Metallization of Zn on the ZnO surface governed the gas sensing mechanism about high response and great selectivity to H_2 at room temperature (Figure 10h–j). Moreover, the synergetic effect of 2D nanosheets and interconnected holey/porous network of ZnO generated the excellent H_2 sensing performances by offering abundant active sites for H_2 molecules.

2.4. MoS_2-Based H_2 Sensors

In recent year, MoS_2 has shown great H_2 sensing potential due to its 2D van der Waals structures, H_2 adsorption capacity and enable RT operation [65,66]. Unfortunately, sluggish response/recovery limited the applications of MoS_2-based H_2 sensors. In regard of this case, some composites based on MoS_2 were investigated for H_2 sensing. Huang and Chen at al [38] designed hybrid interlinked MoS_2-ZnO nanotubes for RT H_2 sensing of 51.1% to 500 ppm with 14/19 s response/recovery and LOD of 10 ppm, due to the increased oxygen vacancies and surface-active sites. Hollow MoS_2/Pt-based chemiresistors, designed by Kim et al. [65], exhibited great H_2 sensing performance with fast response/recovery rate at RT (8.1/16 s for 1%, and 2.7/16 s for 4% H_2), due to the catalytic H_2 spillover of Pt, as well as sufficiently permeable pathways and maximized active sites for H_2 produced by the hollow MoS_2. Similarly, vertically aligned edge-oriented Pd/MoS_2 nanofilm was reported for great H_2 sensing properties at RT, response of 33.7% to 500 ppm with response/recovery of 16 s/38 s, and LOD of 50 ppm [66]. Even so, selectivity of RT H_2 sensors based on MoS_2 has not been investigated widely and deeply.

2.5. Other-Based H_2 Sensors

With the development of nanoscience and nanotechnology, new composites for RT H_2 sensors have been developed. Xu and Ou et al. [67] explored ultrathin nickel oxysulfide which exhibited a selective and fully reversible response to H_2 at RT for a wide range from 0.25% to 1%, due to the physisorption of H_2 on the surface. Dash et al. [68] developed RT H_2 sensors based on rGO-$ZnFe_2O_4$-Pd nanocomposite, showing high sensitivity and fast response/recovery rate (11.43% to 200 ppm with 18/29 s response/recovery) to a wide range of H_2 (50–1000 ppm), due to the synergistic effect of rGO, $ZnFe_2O_4$ and Pd nanoparticles.

Up to now, there are lots of efforts to develop room temperature resistive H_2 sensors. Unfortunately, no H_2 sensors integrated inside of LIB cells have been reported. Table 1 summarizes the recent and representative room temperature resistive H_2 sensors possibly integrated inside of LIB cells. Although new gas sensing materials are emerging all of the time, Pd and Pd-based materials have been the current state-of-the-art resistive H_2 sensing material operating at room temperature. In conclusion, Pd is still the most excellent catalyst for RT H_2 sensing with great selectivity due to the formation of PdH_x. But the LOD (ppm level) and response/recovery behavior (tens of seconds) of Pd-based H_2 sensors should be further improved. Sensors based on Pd-carbon materials should be state-of-the-art RT H_2 sensors displaying LOD of ppb-level (due to the catalytic H_2 adsorption/dissociation on Pd surface, as well as high surface area and RT good conductivity of carbon materials). However, they still suffer from slow response/recovery rate (tens of seconds) to ppb-H_2 at RT. According to previous investigations, atomically dispersed sub-nano clusters (perhaps single atom) of Pd are in favor of ppb-level H_2 detection at RT; optimal d-band energy level of Pd could yield complete and fast recovery; construction of conduction channel in Pd-based sensing material could generate fast response and recovery rate. Although some composites of MOXs exhibited good RT H_2 sensing property, they inherently showed cross-sensitivity to other gases (such as NO_2, CO and ethanol) and susceptibility to humidity. Despite some new structures and materials (ternary composites, MoS_2, and MXene) emerging for RT H_2 sensing, fast response in 1 s to ppb-H_2 with special selectivity is still a critical issue.

3. Selectivity

LIBs usually undergo the following changes with abuse: lithium precipitation at the negative electrode, decomposition of solid electrolyte interface (SEI) layer, melting of the separator, reaction of electrolyte with anode, decomposition of the positive electrode, decomposition, and vaporization of the electrolyte [8]. Multiple side reactions can occur simultaneously, producing gas mixture, including H_2, CO, water vapor, and electrolyte vapors. Therefore, selectivity of H_2 sensors inside of LIB is a critical issue for the early safety warning of LIBs.

Chemo-resistive H_2 sensors generally suffer from cross-sensitivity with other gases (for example, CO, hydrocarbon gases, water vapor, ethanol vapor, and NO_2). Synergistic effect of heterogeneous composite, adjustment of dangling bonds on the sensing material surface, and filter membrane are conventional means to improve the selective response to H_2. Pd has been extensively decorated on the major sensing materials to improve the H_2 selectivity, due to the high H_2 adsorption capacity [37]. Heterogeneous composites of MOX-MOX, MOX-carbon material, and MOX-MoS_2 were usually developed for great selective H_2 response due to the synergistic effect of heterojunctions. In our previous report [69], reducing the surface oxygen-containing functional groups via heat treatment under H_2 condition was verified to improve the H_2 selectivity by inhibiting the intercross response to oxidizing gas (NO_2) and organic gas (ethanol). As one of the obstinate problems for room temperature resistive gas sensors, humidity interference has been troubling researchers in decades. The humidity-resistant properties of Ag_2Te-based NO_2 sensor operating at room temperature was demonstrated in a recent report [70]. Adelung and Lupan et al. [71] developed ZnO-based H_2 sensor employing graphene oxide as molecular sieve (Figure 11a). The nanopores in the GO membrane, acting as a size-selective sieve, only allowed permeation of H_2 molecules among the tested gases (ethanol, methane, ammonia, acetone, methanol and H_2). In other reports [24,72], poly(methyl methacrylate) (PMMA) membrane layers have demonstrated the selective H_2 filtration effect, as shown in Figure 11b,c. ZIF-8 membrane has also been investigated to improve H_2 sensing selectivity [55]. Since the pore size of ZIF-8 is 0.34 nm, which is larger than the diffusion kinetic diameter of H_2 molecule (0.289 nm), but a little smaller than that of the other tested gases. For the internal H_2 sensor working under harsh conditions, filling of interface gases (electrolyte vapors, CO, et al.) in the filter membrane could be a better method to inhibit inter-cross selectivity.

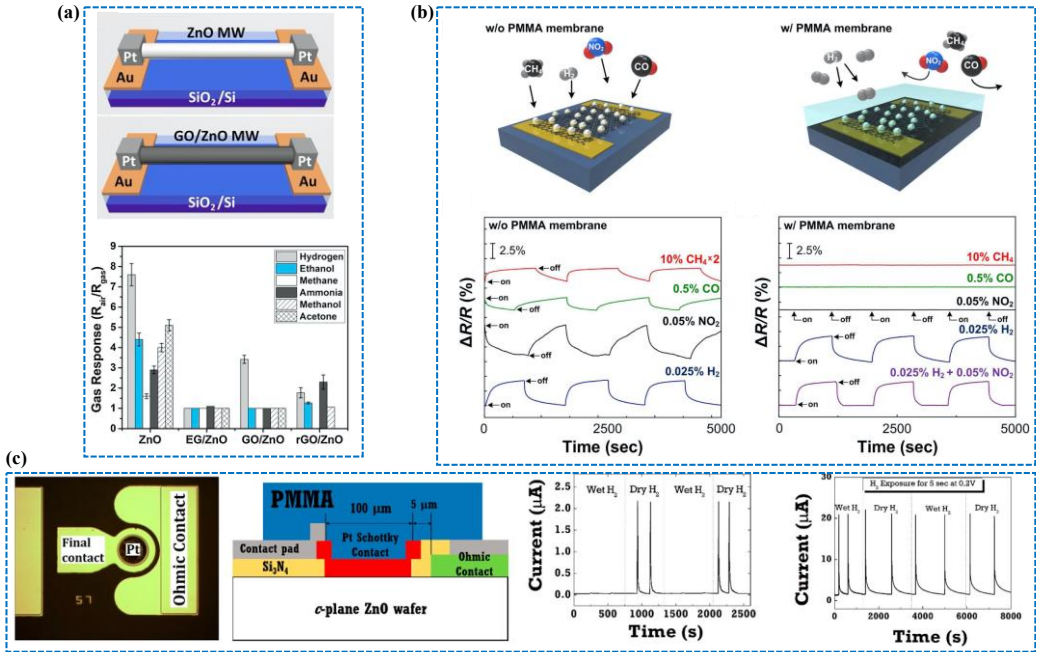

Figure 11. (**a**) Schematic illustration of sensor device based on ZnO microwire and GO/ZnO microwire, and their comparison of selectivity to hydrogen, ethanol, methane, ammonia, methanol, and acetone [71]. Copyright 2020 with permission from Elsevier, open access. (**b**) Schematic illustration of sensor device based on Pd nanoparticle/graphene with and without PMMA coating, and their comparison of selectivity to H_2, CO, and NO_2 [72]. Copyright © 2015 American Chemical Society. (**c**) Optical image and schematic illustration of ZnO-based H_2 sensor with PMMA membrane and stable response to wet and dry H_2 [24]. Copyright 2020 MDPI, open access.

4. Internal Gas Sensors in LIBs

Internal sensor in LIB is much more efficient and timelier for the early safety warning of LIBs. Internal sensors about temperature detection (Figure 12a) [73], and the flexible three-in-one microsensor of internal temperature, voltage and current detection (Figure 12b) [74] have been reported. Unfortunately, to the best of our knowledge, the internal gas sensors (including H_2 sensor) have not been reported yet. Internal gas sensors in LIB should be flexible, stable under serious condition filling with electrolyte vapors and poor air, while operating at room temperature. Flexible gas sensors, including H_2 sensors, have been widely investigated [35,45,53,75,76].

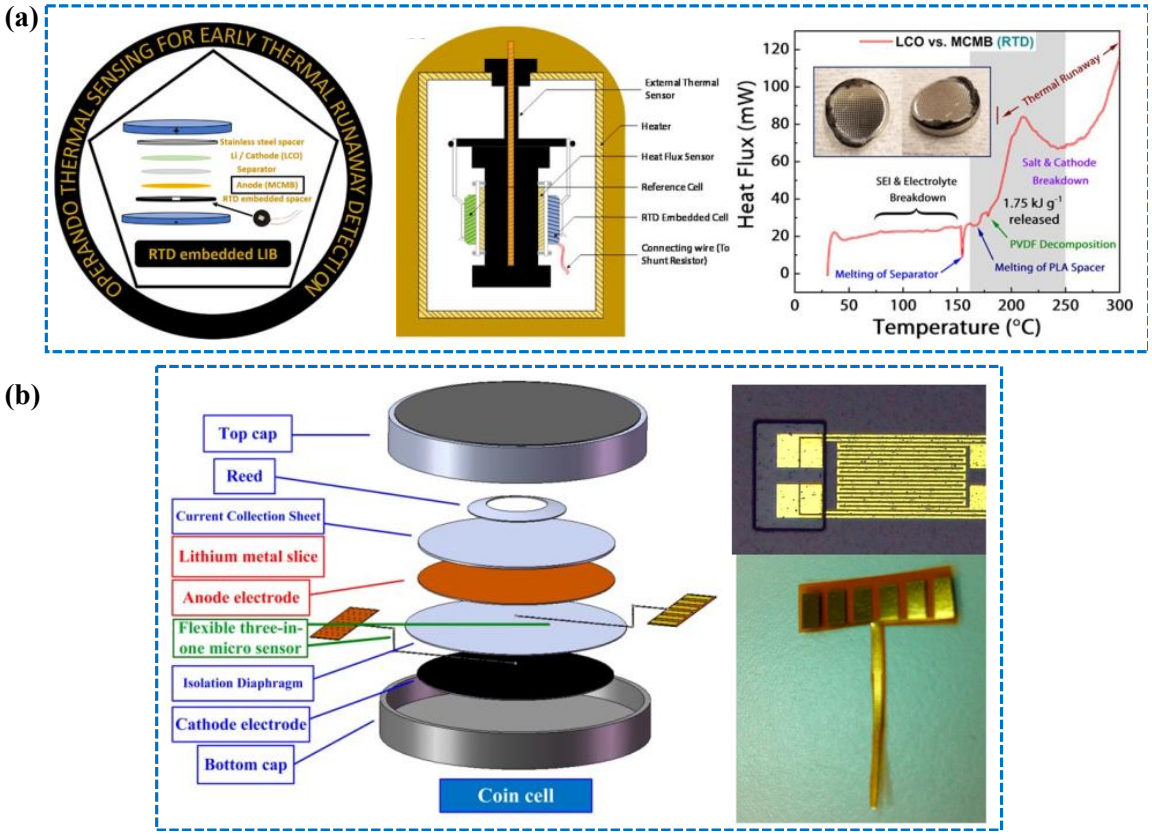

Figure 12. (**a**) Schematical illustration of resistance temperature detector (RTD) embedded in LIB, and the multimode calorimetry (MMC) signal [73]. Copyright © 2020, American Chemical Society. (**b**) Schematic diagram of flexible three-in-one microsensors (temperature, voltage, and current) embedded in a coin cell battery, and the optical micrograph of the flexible three-in-one microsensor [74]. Copyright 2015 with permission from MDPI, open access.

Lee et al. [24] demonstrated that a PMMA membrane coating on Pd-graphene sensing layer could prevent the NO_2, CO and CH_4 response completely (Figure 11b). Li et al. [77] developed Pd-CNTs/PDMS/POTS (PDMS, polydimethylsiloxane; POTS, 1H,1H,2H,2H-perfluorooctyltriethoxysilane) sensors for self-cleaning and humidity-insensitive H_2 sensors at RT. Superhydrophobicity of PDMS/POTS generated the waterproof and self-cleaning properties of the sensor, maintaining the H_2 sensing capacity under highly humidity conditions. Moreover, the self-healing of superhydrophobicity yield the long-term stability of the sensor (Figure 13a). In the work of flexible NO_2 sensor [78], semipermeable PDMS membrane was used to achieve the water-resistant property with an ultralow LOD of 8.3 ppb (Figure 13b). The research on internal H_2 sensor inside of LIB cell could be inspired by plenty of the flexible gas sensor research. A flexible thin film sensor with self-cleaning and H_2 permeable membrane could generate long-term stability inside of LIB cell.

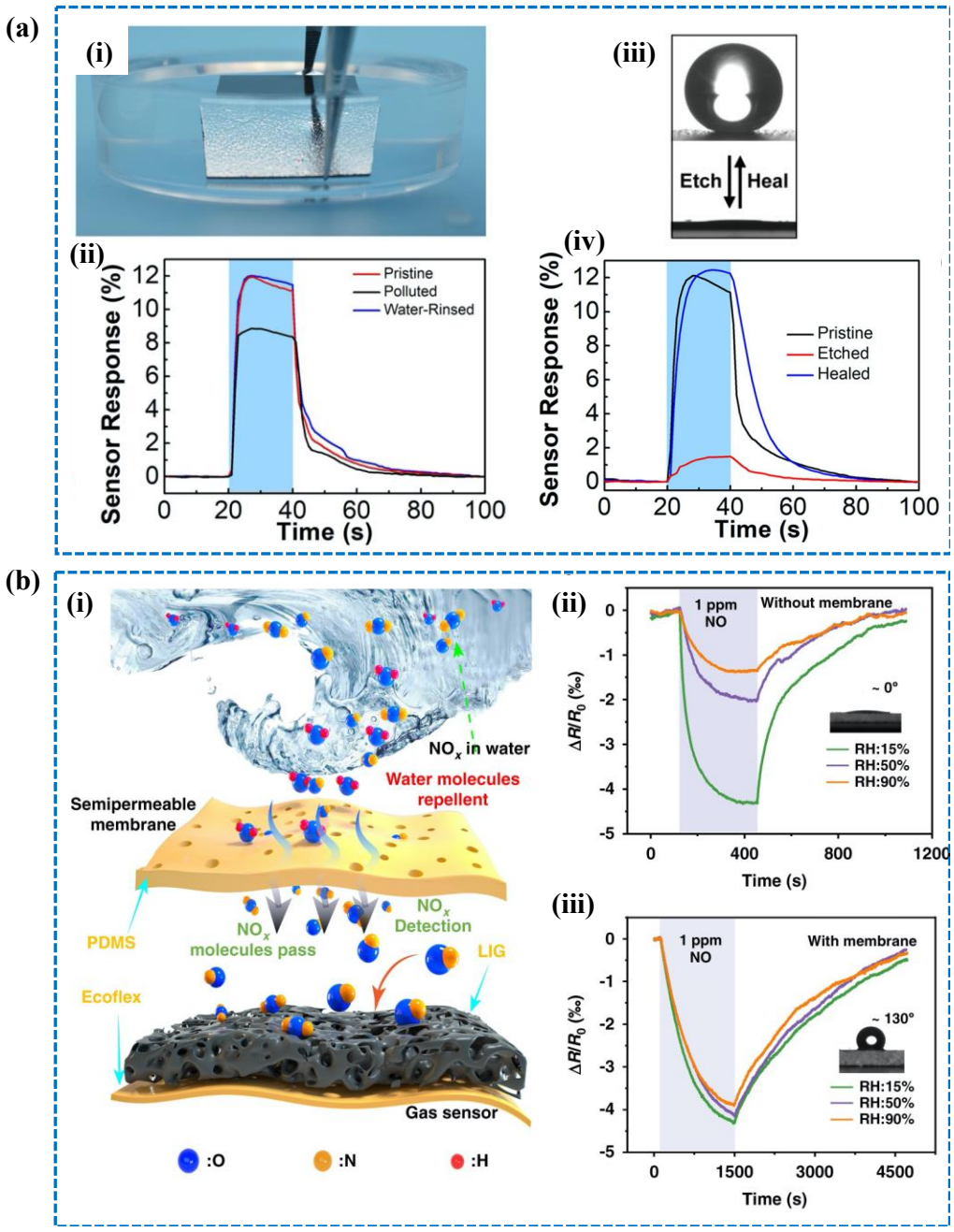

Figure 13. (**a**) H_2 sensing behaviors of CNTs/PDMS/POTS showing self-cleaning and self-healing properties. (**i**) Immersed in water and (**ii**) real-time response to 10 000 ppm H_2 after immersed in water. (**iii**) Reversible change of superhydrophobic (TOP) and superhydrophilic (Bottom) upon O_2 plasma-etching and self-healing and (**iv**) real-time response to 10 000 ppm H_2 after plasma-ethcing and self-healing. [77] Copyright 2021 with permission from Elsevier. (**b**) (**i**) Schematic illustration of flexible NO_x sensor operating at RT with PDMS membrane showing waterproof property, and the real-time response to 1 ppm NO_2 under different humidity conditions: (**ii**) of the sensor without PDMS membrane and (**iii**) of the sensor with PDMS membrane. [78]. Copyright © 2022, Nature, open access.

Table 1 summarizes the recent and representative resistive H_2 sensors operating at room temperature based on inorganic materials.

Table 1. Recent Studies on Resistive H_2 sensors operating at RT.

Material & Morphology	H_2 Response $\lvert R_{H_2} - R_{air}\rvert / R_{air} \times 100\%$	t_{resp}/t_{rec} [b]	LOD [c] (ppm)	Measurement Range	Ref. [d]
Pd nanofiber yarn	1.37% at 0.1%	236 s/388 s at 0.1%	2	1 ppm to 4%	[43]
Pd nanofiber yarn	0.88% at 0.1%	76 s/384 s at 0.1%	1	1 ppm to 4%	[43]
Pd nanopattern	0.8% at 0.1%	230 s/680 s at 0.1%	2.5	2.5 ppm to 4%	[44]
Pd nanotube array	1000% at 0.1%	180 s/n.r. at 0.1%	100	100 ppm to 1%	[45]
Pd/Pt nanopattern	2% at 1%	7 s/35 s at 0.1%	10	10 ppm to 1%	[49]
Pd/Au nanopattern	n.r.	8 s/30 s at 0.1%	10	10 ppm to 1%	[49]
Pd/Mg film	3% at 1%	6 s/32 s at 1%	1	1 ppm to 4%	[50]
Pd–Sn Alloy Nanotube	1.63% at 200 ppm	20 s/18 s at 200 ppm	1	0.5 ppm to 3%	[51]
PdMo alloy nanosheet	18.7% at 1%	73 s/40 s at 1%	1	0.01% to 1%	[35]
Pd-PdO Hollow Shells	4.6% at 1 ppm	5 s/32 s at 1%	1	1 ppm to 1%	[46]
Pd-ZnO nanoflowers	45% at 10 ppm	137 s/165 s at 300 ppb	0.3	0.3 to70 ppm	[37]
Pd/ZnO	39.2% at 1000 ppm	68 s/n.r. at 1000 ppm	1000	0.1% to 2%	[75]
Pd-WO_3 nanoparticle	1786.3 [a] at 100 ppm	41 s/n.r. at 100 ppm	1	1 to 100 ppm	[79]
MWCNT@Pd nanosheets	3.6% at 1%	74 s/35 s at 1%	5	0.02% to 1%	[80]
Pt/g- C_3N_4 film	51% at 10,000 ppm	39 s/5 s to 10,000 ppm	1%	1% to 10%	[81]
Pd-decorated crumpled rGO	14.8% at 2%	73 s/126 s at 2%	25	25 ppm to 2%	[82]
Pd/porous graphene	0.6% at 600 ppm	n.r.	600	600 ppm to 1.3%	[83]
Pd/graphene	66% at 2%	1.8 min/5.5 min at 2%	25	0.025% to 2%	[72]
Pd sub-nano clusters on graphene	15% at 5 ppm	25 s/35 s at 5 ppm	0.05	50 ppb to 5 ppm	[33]
Pd nanowires@ZIF-8 Core-shell	0.8% at 0.1%	8 s/30 s at 0.1% H_2	600	600 ppm to 1%	[55]
Vertically aligned Pd/MoS_2 nanofilm	33.7% at 500 ppm	16 s/38 s at 500 ppm	50	50 ppm to 1%	[66]
Pd-sodium titanate nanoribbons	12.0 [a] to 1%	1.1 s/13.5 s at 1%	0.8	0.8 ppm to 10%	[54]
Pd- sodium titanate nanoparticles	5.7 [a] to 1%	13.3 s/39 s at 1%	100	100 ppm to 5%	[54]
$Ti_3C_2T_x$@Pd nanoclusters	23% at 4%	32 s/161 s at 4%	0.5%	0.5% to 40%	[53]
rGO-$ZnFe_2O_4$–Pd	11.43% to 200 ppm	18 s/39 s at 200 ppm	50	50 to 1000 ppm	[68]
Pt/rGO	97% at 500 ppm	65 s/230 s at 5000 ppm	200	200 to 5000 ppm	[57]
Pt/3D graphene	6.1% at 1%	25 s/20 s at 1%	10	10 ppm to 1%	[59]
Pt-PdO nanowires	23% at 100 ppm	166 s/445 s at 0.1%	10	10 to 100 ppm	[84]
Au@PdO nanoparticle arrays	~180 [a] at 1%	n.r.	0.1	0.1 ppm to 1%	[36]
PdO-PdAu Ternary Hollow Shells	n.r.	2.2 s/23 s at 0.1%	30	30 ppm to 1%	[85]
Hollow MoS_2/Pt	8.7% at 1%	8 s/16 s at 1%	500	500 ppm to 4%	[65]
2D holey ZnO	115% at 100 ppm	9 s/6 s at 100 ppm	5	5 to 100 ppm	[39]
WO_3-TiO_2 composite	5.62 [a] at 10,000 ppm	48 s/5 s at 10,000 ppm	1000	1000 to 10,000 ppm	[63]
MoS_2-ZnO nanotubes	0.51 [a] at 500 ppm	14 s/19 s at 500 ppm	10	10 to 500 ppm	[38]
SnO_2-coated β-Ga_2O_3 nanobelts	115% at 33 ppm	216 s/125 s at 33 ppm	33	33 to 1000 ppm	[64]
Nanocrystalline SnO_2 thin film	48% at 3 ppm	135 s/46 s at 3 ppm	3	3 to 100 ppm	[60]
Well-aligned MoO_3 nanoribbon arrays	~3% at 100 ppm	3 s/16 s at 100 ppm	100	100 to 500 ppm	[61]
ZnO microwires with GO membrane	3.42 [a] at 1000 ppm	114 s/30 s at 1000 ppm	10	10 to 1000 ppm	[71]
ordered mesoporous TiO_2	298 [a] at 1000 ppm	85 s/198 s at 1000 ppm	100	100 to 1000 ppm	[62]
3D nickel oxysulfide micro-flowers	3.24% at 1%	20 min/33 min to 1%	0.25%	0.25% to 1%	[67]

n.r. indicates not reported. [a] Response is defined as R_{H_2}/R_{air}. [b] Response is defined as the time taken from baseline to 90% of the maximum response; recovery time is defined as the time taken from the maximum response to 10% of maximum response. [c] LOD is the limit of detection measured by experiment. [d] Ref. is the reference number.

5. Conclusions and Perspective

H_2 detection inside lithium-ion battery cells is the most effective measure for the early safety warning of LIBs. The special application condition proposed special requirements for H_2 sensors in terms of working at room temperature, response time, detection concentration, selectivity, stability, and even packaging.

Gas sensing material is the core of a gas sensor. In the past few decades, chemiresistive RT H_2 sensors based on various materials were investigated, including noble metals (Pd, Pt), metal oxides (ZnO, SnO_2, TiO_2, et al.), carbon materials (CNT, graphene, C_3N_4), MoS_2,

MXene, and their composites. For each material, various approaches were studied to improve the H_2 sensing performances, such as morphology and structure design, catalyst addition, as well as establishment of heterojunctions. Obviously, Pd and Pd-based materials has been still the current state-of-the-art room temperature resistive H_2 sensing material. Although the LOD (ppm level) and response/recovery behavior (tens of seconds) of room temperature H_2 sensors has been developed, further exploration for the H_2 sensor experimentally applied for early safety warning of LIBs is required.

Thin H_2 sensor integrated inside of LIB cell could be much more efficient and timelier for the early safety warning of LIBs, which has not been reported yet. Great selectivity to H_2 is required for the H_2 sensor integrated in LIB cell, especially inhibiting the inter-cross sensitivity to electrolyte vapors. Sensor device covered by semipermeable membrane is promising and necessary for the internal gas sensor in LIB to prevent the device from electrolyte vapors and other gases released from the chemical reactions inside the battery while also improving long-term stability.

Research concerning resistive H_2 sensors integrated inside of LIB cells for early safety warning is still in an early stage. Notably, both the physical stability and the sensing stability of the internal gas sensor in a few years are crucial.

We overviewed the recently interesting advances of resistive H_2 sensors possibly used inside of LIB. Although there remain huge challenges and unexplored topics, we strongly believe that the resistive H_2 sensors will further grow in the future and unlock novel applications in LIBs. We hope that this review inspired the applications of H_2 sensors in early safety warning of LIBs.

Author Contributions: Writing—original draft, S.L., S.Z. (Shuaiyin Zhao) and Z.C. Writing—Review and Editing, S.Z. (Shiyu Zhou) and W.Y. Figures, S.Z. (Shuaiyin Zhao) and T.J. Literature retrieval, T.J., M.Z. and P.G. Funding acquisition, W.Y. Supervision, W.Y. and M.L. All authors have read and agreed to the published version of the manuscript.

Funding: This research was supported by the National Science and Technology Foundation (62201185).

Institutional Review Board Statement: The study did not require ethical approval.

Informed Consent Statement: This study did not involve humans.

Acknowledgments: Y.W.J. acknowledges the 2011 Zhejiang Regional Collaborative Innovation Centre for Smart City.

Conflicts of Interest: The authors declare no conflict of interest.

References

1. Goodenough, J.B.; Park, K.-S. The Li-ion rechargeable battery: A perspective. *J. Am. Chem. Soc.* **2013**, *135*, 1167–1176. [CrossRef] [PubMed]
2. Tarascon, J.M.; Armand, M. Issues and challenges facing rechargeable lithium batteries. *Nature* **2001**, *414*, 359–367. [CrossRef] [PubMed]
3. Armand, M.; Tarascon, J.M. Building better batteries. *Nature* **2008**, *451*, 652–657. [CrossRef] [PubMed]
4. Choi, J.W.; Aurbach, D. Promise and reality of post-lithium-ion batteries with high energy densities. *Nat. Rev. Mater.* **2016**, *1*, 16013. [CrossRef]
5. Niu, H.; Wang, L.; Guan, P.; Zhang, N.; Yan, C.; Ding, M.; Guo, X.; Huang, T.; Hu, X. Recent advances in application of ionic liquids in electrolyte of lithium ion batteries. *J. Energy Storage* **2021**, *40*, 102659. [CrossRef]
6. Liu, K.; Liu, Y.; Lin, D.; Pei, A.; Cui, Y. Materials for lithium-ion battery safety. *Sci. Adv.* **2018**, *4*, eaas9820. [CrossRef]
7. Jin, Y.; Zheng, Z.K.; Wei, D.H.; Jiang, X.; Lu, H.F.; Sun, L.; Tao, F.B.; Guo, D.L.; Liu, Y.; Gao, J.F.; et al. Detection of Micro-Scale Li Dendrite via H_2 Gas Capture for Early Safety Warning. *Joule* **2020**, *4*, 1714–1729. [CrossRef]
8. Shi, S.; Lyu, N.; Jiang, X.; Song, Y.; Lu, H.; Jin, Y. Hydrogen gas diffusion behavior and detector installation optimization of lithium ion battery energy-storage cabin. *J. Energy Storage* **2023**, *67*, 107510. [CrossRef]
9. Zhao, H.; Wang, J.; Shao, H.; Xu, K.; Deng, Y. Gas Generation Mechanism in Li-Metal Batteries. *Energy Environ. Mater.* **2022**, *5*, 327–336. [CrossRef]
10. Liao, Z.H.; Zhang, S.; Li, K.; Zhang, G.Q.; Habetler, T.G. A survey of methods for monitoring and detecting thermal runaway of lithium-ion batteries. *J. Power Sources* **2019**, *436*, 226879. [CrossRef]

11. Guo, X.; Guo, S.; Wu, C.; Li, J.; Liu, C.; Chen, W. Intelligent Monitoring for Safety-Enhanced Lithium-Ion/Sodium-Ion Batteries. *Adv. Energy Mater.* **2023**, *13*, 2203903. [CrossRef]
12. Kaur, P.; Bagchi, S.; Gribble, D.; Pol, V.G.; Bhondekar, A.P. Impedimetric Chemosensing of Volatile Organic Compounds Released from Li-Ion Batteries. *ACS Sens.* **2022**, *7*, 674–683. [CrossRef] [PubMed]
13. Cai, T.; Valecha, P.; Tran, V.; Engle, B.; Stefanopoulou, A.; Siegel, J. Detection of Li-ion battery failure and venting with Carbon Dioxide sensors. *Etransportation* **2021**, *7*, 100100. [CrossRef]
14. Santos-Carballal, D.; Lupan, O.; Magariu, N.; Ababii, N.; Kruger, H.; Bodduluri, M.T.; de Leeuw, N.H.; Hansen, S.; Adelung, R. Al_2O_3/ZnO composite-based sensors for battery safety applications: An experimental and theoretical investigation. *Nano Energy* **2023**, *109*, 108301. [CrossRef]
15. Essl, C.; Seifert, L.; Rabe, M.; Fuchs, A. Early detection of failing automotive batteries using gas sensors. *Batteries* **2021**, *7*, 25. [CrossRef]
16. Mateev, V.; Marinova, I.; Kartunov, Z. Gas Leakage Source Detection for Li-Ion Batteries by Distributed Sensor Array. *Sensors* **2019**, *19*, 2900. [CrossRef]
17. Huang, W.; Feng, X.; Pan, Y.; Jin, C.; Sun, J.; Yao, J.; Wang, H.; Xu, C.; Jiang, F.; Ouyang, M. Early warning of battery failure based on venting signal. *J. Energy Storage* **2023**, *59*, 106536. [CrossRef]
18. Zhang, X.; Chen, S.; Zhu, J.; Gao, Y. A Critical Review of Thermal Runaway Prediction and Early-Warning Methods for Lithium-Ion Batteries. *Energy Mater. Adv.* **2023**, *4*, 0008. [CrossRef]
19. Li, B.; Lai, P.T.; Tang, W.M. Influence of Source/Drain Catalytic Metal and Fabrication Method on OTFT-Based Hydrogen Sensor. *IEEE Trans. Electron. Devices* **2022**, *69*, 2038–2042. [CrossRef]
20. Ghosh, S.; Rajan, L.; Varghese, A. Junctionfree Gate Stacked Vertical TFET Hydrogen Sensor at Room Temperature. *IEEE Trans. Nanotechnol.* **2022**, *21*, 655–662. [CrossRef]
21. Zhou, S.; Xiao, M.; Liu, F.; He, J.; Lin, Y.; Zhang, Z. Sub-10 parts per billion detection of hydrogen with floating gate transistors built on semiconducting carbon nanotube film. *Carbon* **2021**, *180*, 41–47. [CrossRef]
22. Skucha, K.; Fan, Z.Y.; Jeon, K.; Javey, A.; Boser, B. Palladium/silicon nanowire Schottky barrier-based hydrogen sensors. *Sens. Actuators B Chem.* **2010**, *145*, 232–238. [CrossRef]
23. Chen, W.-C.; Niu, J.-S.; Liu, I.P.; Liu, B.-Y.; Cheng, S.-Y.; Lin, K.-W.; Liu, W.-C. Room-Temperature Hydrogen- and Ammonia Gas-Sensing Characteristics of a GaN-Based Schottky Diode Synthesized with a Hybrid Surface Structure. *IEEE Trans. Electron. Devices* **2021**, *68*, 761–768. [CrossRef]
24. Jang, S.; Jung, S.; Baik, K.H. Hydrogen sensing performance of ZnO Schottky diodes in humid ambient conditions with PMMA membrane layer. *Sensors* **2020**, *20*, 835. [CrossRef] [PubMed]
25. Ghosh, S.; Rajan, L. Room Temperature Hydrogen Sensing Investigation of Zinc Oxide Schottky Thin-Film Transistors: Dependence on Film Thickness. *IEEE Trans. Electron. Devices* **2020**, *67*, 5701–5709. [CrossRef]
26. Ratan, S.; Kumar, C.; Kumar, A.; Jarwal, D.K.; Mishra, A.K.; Upadhyay, R.K.; Singh, A.P.; Jit, S. Room temperature high hydrogen gas response in Pd/TiO2/Si/Al capacitive sensor. *Micro Nano Lett.* **2020**, *15*, 632–635. [CrossRef]
27. Constantinoiu, I.; Viespe, C. Development of Pd/TiO_2 Porous Layers by Pulsed Laser Deposition for Surface Acoustic Wave H_2 Gas Sensor. *Nanomaterials* **2020**, *10*, 760. [CrossRef]
28. Hosoki, A.; Nishiyama, M.; Sakurai, N.; Igawa, H.; Watanabe, K. Long-Term Hydrogen Detection Using a Hetero-Core Optical Fiber Structure Featuring Au/Ta_2O_5/Pd/Pt Multilayer Films. *IEEE Sens. J.* **2020**, *20*, 227–233. [CrossRef]
29. Dai, J.; Li, Y.; Ruan, H.; Ye, Z.; Chai, N.; Wang, X.; Qiu, S.; Bai, W.; Yang, M. Fiber Optical Hydrogen Sensor Based on WO_3-Pd_2Pt-Pt Nanocomposite Films. *Nanomaterials* **2021**, *11*, 128. [CrossRef]
30. Koo, W.T.; Cho, H.J.; Kim, D.H.; Kim, Y.H.; Shin, H.; Penner, R.M.; Kim, I.D. Chemiresistive Hydrogen Sensors: Fundamentals, Recent Advances, and Challenges. *ACS Nano* **2020**, *14*, 14284–14322. [CrossRef]
31. Favier, F.; Walter, E.C.; Zach, M.P.; Benter, T.; Penner, R.M. Hydrogen sensors and switches from electrodeposited palladium mesowire arrays. *Science* **2001**, *293*, 2227–2231. [CrossRef] [PubMed]
32. Zhou, L.; Li, Z.; Chang, X.; Liu, X.; Hu, Y.; Li, M.; Xu, P.; Pinna, N.; Zhang, J. PdRh-Sensitized Iron Oxide Ultrathin Film Sensors and Mechanistic Investigation by Operando TEM and DFT Calculation. *Small* **2023**, 2301485. [CrossRef] [PubMed]
33. Ahmad, W.; Yan, W.; Ling, M.; Liang, C. DNA-Incorporated Biomimetic Olfactory Neuroepithelium That Facilitates Artificial Intelligence. *Adv. Intell. Syst.* **2023**, 2200396. [CrossRef]
34. Zhu, J.; Cho, M.; Li, Y.; He, T.; Ahn, J.; Park, J.; Ren, T.-L.; Lee, C.; Park, I. Machine learning-enabled textile-based graphene gas sensing with energy harvesting-assisted IoT application. *Nano Energy* **2021**, *86*, 106035. [CrossRef]
35. Kumar, A.; Zhao, Y.; Abraham, S.R.; Thundat, T.; Swihart, M.T. Pd Alloy Nanosheet Inks for Inkjet-Printable H_2 Sensors on Paper. *Adv. Mater. Interfaces* **2022**, *9*, 2200363. [CrossRef]
36. Yang, S.; Li, Q.; Li, C.; Cao, T.; Wang, T.; Fan, F.; Zhang, X.; Fu, Y. Enhancing the Hydrogen-Sensing Performance of p-Type PdO by Modulating the Conduction Model. *ACS Appl. Mater. Interfaces* **2021**, *13*, 52754–52764. [CrossRef]
37. Jeon, J.-Y.; Park, S.-J.; Ha, T.-J. Functionalization of Zinc Oxide Nanoflowers with Palladium Nanoparticles via Microwave Absorption for Room Temperature-Operating Hydrogen Gas Sensors in the ppb Level. *ACS Appl. Mater. Interfaces* **2021**, *13*, 25082–25091. [CrossRef]

38. Vivekanandan, A.K.; Huang, B.-R.; Kathiravan, D.; Saravanan, A.; Prasannan, A.; Tsai, H.-C.; Chen, S.-H. Effect of MoS_2 solution on reducing the wall thickness of ZnO nanotubes to enhance their hydrogen gas sensing properties. *J. Alloys Compd.* **2021**, *854*, 157102. [CrossRef]
39. Kumar, M.; Bhatt, V.; Kim, J.; Abhyankar, A.C.; Chung, H.-J.; Singh, K.; Bin Cho, Y.; Yun, Y.J.; Lim, K.S.; Yun, J.-H. Holey engineered 2D ZnO-nanosheets architecture for supersensitive ppm level H_2 gas detection at room temperature. *Sens. Actuators B Chem.* **2021**, *326*, 128839. [CrossRef]
40. Wang, C.; Zhou, G.; Li, J.; Yan, B.; Duan, W. Hydrogen-induced metallization of zinc oxide (2 1 1 0) surface and nanowires: The effect of curvature. *Phys. Rev. B.* **2008**, *77*, 245303. [CrossRef]
41. Sakintuna, B.; Lamari-Darkrim, F.; Hirscher, M. Metal hydride materials for solid hydrogen storage: A review. *Int. J. Hydrogen Energy* **2007**, *32*, 1121–1140. [CrossRef]
42. Xu, T.; Zach, M.; Xiao, Z.; Rosenmann, D.; Welp, U.; Kwok, W.; Crabtree, G. Self-assembled monolayer-enhanced hydrogen sensing with ultrathin palladium films. *Appl. Phys. Lett.* **2005**, *86*, 203104. [CrossRef]
43. Kim, D.H.; Kim, S.J.; Shin, H.; Koo, W.T.; Jang, J.S.; Kang, J.Y.; Jeong, Y.J.; Kim, I.D. High-Resolution, Fast, and Shape-Conformable Hydrogen Sensor Platform: Polymer Nanofiber Yarn Coupled with Nanograined Pd@Pt. *ACS Nano* **2019**, *13*, 6071–6082. [CrossRef] [PubMed]
44. Cho, S.Y.; Ahn, H.; Park, K.; Choi, J.; Kang, H.; Jung, H.T. Ultrasmall Grained Pd Nanopattern H_2 Sensor. *ACS Sens.* **2018**, *3*, 1876–1883. [CrossRef] [PubMed]
45. Lim, M.A.; Kim, D.H.; Park, C.O.; Lee, Y.W.; Han, S.W.; Li, Z.Y.; Williams, R.S.; Park, I. A New Route toward Ultrasensitive, Flexible Chemical Sensors: Metal Nanotubes by Wet-Chemical Synthesis along Sacrificial Nanowire Templates. *ACS Nano* **2012**, *6*, 598–608. [CrossRef] [PubMed]
46. Gao, Z.; Wang, T.; Li, X.; Li, Q.; Zhang, X.; Cao, T.; Li, Y.; Zhang, L.; Guo, L.; Fu, Y. Pd-Decorated PdO Hollow Shells: A H_2-Sensing System in Which Catalyst Nanoparticle and Semiconductor Support are Interconvertible. *ACS Appl. Mater. Interfaces* **2020**, *12*, 42971–42981. [CrossRef] [PubMed]
47. Li, X.W.; Liu, Y.; Hemminger, J.C.; Penner, R.M. Catalytically Activated Palladium@Platinum Nanowires for Accelerated Hydrogen Gas Detection. *ACS Nano* **2015**, *9*, 3215–3225. [CrossRef]
48. Yang, F.; Kung, S.-C.; Cheng, M.; Hemminger, J.C.; Penner, R.M. Smaller is faster and more sensitive: The effect of wire size on the detection of hydrogen by single palladium nanowires. *ACS Nano* **2010**, *4*, 5233–5244. [CrossRef]
49. Jung, W.B.; Cho, S.Y.; Suh, B.L.; Yoo, H.W.; Jeon, H.J.; Kim, J.; Jung, H.T. Polyelemental nanolithography via plasma ion bombardment: From fabrication to superior H2 sensing application. *Adv. Mater.* **2019**, *31*, 1805343. [CrossRef]
50. Hassan, K.; Chung, G.S. Fast and reversible hydrogen sensing properties of Pd-capped Mg ultra-thin films modified by hydrophobic alumina substrates. *Sens. Actuators B Chem.* **2017**, *242*, 450–460. [CrossRef]
51. Song, L.; Ahn, J.; Kim, D.-H.; Shin, H.; Kim, I.-D. Porous Pd-Sn Alloy Nanotube-Based Chemiresistor for Highly Stable and Sensitive H_2 Detection. *ACS Appl. Mater. Interfaces* **2022**, *14*, 28378–28388. [CrossRef] [PubMed]
52. Sun, S.; Zhou, X.; Cong, B.; Hong, W.; Chen, G. Tailoring the d-Band Centers Endows $(Ni_xFe_{1-x})_2P$ Nanosheets with Efficient Oxygen Evolution Catalysis. *ACS Catal.* **2020**, *10*, 9086–9097. [CrossRef]
53. Zhu, Z.; Liu, C.; Jiang, F.; Liu, J.; Ma, X.; Liu, P.; Xu, J.; Wang, L.; Huang, R. Flexible and lightweight Ti_3C_2Tx MXene@Pd colloidal nanoclusters paper film as novel H_2 sensor. *J. Hazard. Mater.* **2020**, *399*, 123054. [CrossRef] [PubMed]
54. Wu, J.; Guo, Y.; Wang, Y.; Zhu, H.; Zhang, X. Ti_3C_2 MXene-derived sodium titanate nanoribbons for conductometric hydrogen gas sensors. *Sens. Actuators B Chem.* **2022**, *361*, 131693. [CrossRef]
55. Koo, W.T.; Qiao, S.; Ogata, A.F.; Jha, G.; Jang, J.S.; Chen, V.T.; Kim, I.D.; Penner, R.M. Accelerating Palladium Nanowire H(2) Sensors Using Engineered Nanofiltration. *ACS Nano* **2017**, *11*, 9276–9285. [CrossRef]
56. Greeley, J.; Mavrikakis, M. Surface and subsurface hydrogen: Adsorption properties on transition metals and near-surface alloys. *J. Phys. Chem. B.* **2005**, *109*, 3460–3471. [CrossRef]
57. Ghosh, R.; Santra, S.; Ray, S.K.; Guha, P.K. Pt-functionalized reduced graphene oxide for excellent hydrogen sensing at room temperature. *Appl. Phys. Lett.* **2015**, *107*, 153102. [CrossRef]
58. Kim, Y.; Choi, Y.S.; Park, S.Y.; Kim, T.; Hong, S.P.; Lee, T.H.; Moon, C.W.; Lee, J.H.; Lee, D.; Hong, B.H.; et al. Au decoration of a graphene microchannel for self-activated chemoresistive flexible gas sensors with substantially enhanced response to hydrogen. *Nanoscale* **2019**, *11*, 2966–2973. [CrossRef]
59. Phan, D.-T.; Youn, J.-S.; Jeon, K.-J. High-sensitivity and fast-response hydrogen sensor for safety application using Pt nanoparticle-decorated 3D graphene. *Renew. Energy* **2019**, *144*, 167–171. [CrossRef]
60. Kadhim, I.H.; Abu Hassan, H.; Ibrahim, F.T. Hydrogen gas sensing based on nanocrystalline SnO2 thin films operating at low temperatures. *Int. J. Hydrogen Energy* **2020**, *45*, 25599–25607. [CrossRef]
61. Yang, P.; Li, X.; Huang, H.; Yang, S.; Zhang, X.; Hu, Y.; Wang, Z.; Gu, H. Hydrogen sensing kinetics of laterally aligned MoO_3 nanoribbon arrays with accelerated response and recovery performances at room temperature. *Int. J. Hydrogen Energy* **2020**, *45*, 23841–23850. [CrossRef]
62. Haidry, A.A.; Xie, L.; Wang, Z.; Li, Z. Hydrogen sensing and adsorption kinetics on ordered mesoporous anatase TiO_2 surface. *Appl. Surf. Sci.* **2020**, *500*, 144219. [CrossRef]
63. Li, H.; Wu, C.-H.; Liu, Y.-C.; Yuan, S.-H.; Chiang, Z.-X.; Zhang, S.; Wu, R.-J. Mesoporous WO_3-TiO_2 heterojunction for a hydrogen gas sensor. *Sens. Actuators B Chem.* **2021**, *341*, 130035. [CrossRef]

64. Abdullah, Q.N.; Ahmed, A.R.; Ali, A.M.; Yam, F.K.; Hassan, Z.; Bououdina, M. Novel SnO_2-coated beta-Ga_2O_3 nanostructures for room temperature hydrogen gas sensor. *Int. J. Hydrogen Energy* **2021**, *46*, 7000–7010. [CrossRef]
65. Park, C.H.; Koo, W.-T.; Lee, Y.J.; Kim, Y.H.; Lee, J.; Jang, J.-S.; Yun, H.; Kim, I.-D.; Kim, B.J. Hydrogen Sensors Based on MoS_2 Hollow Architectures Assembled by Pickering Emulsion. *ACS Nano* **2020**, *14*, 9652–9661. [CrossRef]
66. Jaiswal, J.; Tiwari, P.; Singh, P.; Chandra, R. Fabrication of highly responsive room temperature H_2 sensor based on vertically aligned edge-oriented MoS2 nanostructured thin film functionalized by Pd nanoparticles. *Sens. Actuators B Chem.* **2020**, *325*, 128800. [CrossRef]
67. Ha, N.; Xu, K.; Cheng, Y.; Ou, R.; Ma, Q.; Hu, Y.; Vien, T.; Ren, G.; Yu, H.; Zhang, L.; et al. Self-Assembly of Ultrathin Nickel Oxysulfide for Reversible Gas Sensing at Room Temperature. *Chemosensors* **2022**, *10*, 372. [CrossRef]
68. Achary, L.S.K.; Maji, B.; Kumar, A.; Ghosh, S.P.; Kar, J.P.; Dash, P. Efficient room temperature detection of H_2 gas by novel ZnFe2O4-Pd decorated rGO nanocomposite. *Int. J. Hydrogen Energy* **2020**, *45*, 5073–5085. [CrossRef]
69. Zhou, S.; Ji, J.; Qiu, T.; Wang, L.; Ni, W.; Li, S.; Yan, W.; Ling, M.; Liang, C. Boosting selective H_2 sensing of ZnO derived from ZIF-8 by rGO functionalization. *Inorg. Chem. Front.* **2022**, *9*, 599–606. [CrossRef]
70. Yuan, Z.; Zhao, Q.; Duan, Z.; Xie, C.; Duan, X.; Li, S.; Ye, Z.; Jiang, Y.; Tai, H. Ag_2Te nanowires for humidity-resistant trace-level NO_2 detection at room temperature. *Sens. Actuators B Chem.* **2022**, *363*, 131790. [CrossRef]
71. Rasch, F.; Postica, V.; Schutt, F.; Mishra, Y.K.; Nia, A.S.; Lohe, M.R.; Feng, X.; Adelung, R.; Lupan, O. Highly selective and ultra-low power consumption metal oxide based hydrogen gas sensor employing graphene oxide as molecular sieve. *Sens. Actuators B Chem.* **2020**, *320*, 128363. [CrossRef]
72. Hong, J.; Lee, S.; Seo, J.; Pyo, S.; Kim, J.; Lee, T. A Highly Sensitive Hydrogen Sensor with Gas Selectivity Using a PMMA Membrane-Coated Pd Nanoparticle/Single-Layer Graphene Hybrid. *ACS Appl. Mater. Interfaces* **2015**, *7*, 3554–3561. [CrossRef] [PubMed]
73. Parekh, M.H.; Li, B.; Palanisamy, M.; Adams, T.E.; Tomar, V.; Pol, V.G. In situ thermal runaway detection in lithium-ion batteries with an integrated internal sensor. *ACS Appl. Energy Mater.* **2020**, *3*, 7997–8008. [CrossRef]
74. Lee, C.-Y.; Peng, H.-C.; Lee, S.-J.; Hung, I.-M.; Hsieh, C.-T.; Chiou, C.-S.; Chang, Y.-M.; Huang, Y.-P. A flexible three-in-one microsensor for real-time monitoring of internal temperature, voltage and current of lithium batteries. *Sensors* **2015**, *15*, 11485–11498. [CrossRef] [PubMed]
75. Pathak, P.; Cho, H.J. Self-Assembled 1-Octadecanethiol Membrane on Pd/ZnO for a Selective Room Temperature Flexible Hydrogen Sensor. *Micromachines* **2022**, *13*, 26. [CrossRef]
76. Ou, L.X.; Liu, M.Y.; Zhu, L.Y.; Zhang, D.W.; Lu, H.L. Recent Progress on Flexible Room-Temperature Gas Sensors Based on Metal Oxide Semiconductor. *Nanomicro Lett.* **2022**, *14*, 206. [CrossRef]
77. Li, X.; Gao, Z.; Li, B.; Zhang, X.; Li, Y.; Sun, J. Self-healing superhydrophobic conductive coatings for self-cleaning and humidity-insensitive hydrogen sensors. *Chem. Eng. J.* **2021**, *410*, 128353. [CrossRef]
78. Yang, L.; Zheng, G.H.; Cao, Y.Q.; Meng, C.Z.; Li, Y.H.; Ji, H.D.; Chen, X.; Niu, G.Y.; Yan, J.Y.; Xue, Y.; et al. Moisture-resistant, stretchable NO_x gas sensors based on laser-induced graphene for environmental monitoring and breath analysis. *Microsyst. Nanoeng.* **2022**, *8*, 78. [CrossRef]
79. Lee, J.; Kim, S.Y.; Yoo, H.S.; Lee, W. Pd-WO_3 chemiresistive sensor with reinforced self-assembly for hydrogen detection at room temperature. *Sens. Actuators B Chem.* **2022**, *368*, 132236. [CrossRef]
80. Kumar, A.; Zhao, Y.; Mohammadi, M.M.; Liu, J.; Thundat, T.; Swihart, M.T. Palladium Nanosheet-Based Dual Gas Sensors for Sensitive Room-Temperature Hydrogen and Carbon Monoxide Detection. *ACS Sens.* **2022**, *7*, 225–234. [CrossRef]
81. Ibrahim, A.; Memon, U.B.; Duttagupta, S.P.; Raman, R.K.S.; Sarkar, A.; Pendharkar, G.; Tatiparti, S.S.V. Hydrogen gas sensing of nano-confined Pt/g-C3N4 composite at room temperature. *Int. J. Hydrogen Energy* **2021**, *46*, 23962–23973. [CrossRef]
82. Mohammadi, M.M.; Kumar, A.; Liu, J.; Liu, Y.; Thundat, T.; Swihart, M.T. Hydrogen Sensing at Room Temperature Using Flame-Synthesized Palladium-Decorated Crumpled Reduced Graphene Oxide Nanocomposites. *ACS Sens.* **2020**, *5*, 2344–2350. [CrossRef] [PubMed]
83. Zhu, J.; Cho, M.; Li, Y.; Cho, I.; Suh, J.-H.; Orbe, D.D.; Jeong, Y.; Ren, T.-L.; Park, I. Biomimetic turbinate-like artificial nose for hydrogen detection based on 3D porous laser-induced graphene. *ACS Appl. Mater. Interfaces* **2019**, *11*, 24386–24394. [CrossRef] [PubMed]
84. Cho, H.J.; Chen, V.T.; Qiao, S.P.; Koo, W.T.; Penner, R.M.; Kim, I.D. Pt-Functionalized PdO Nanowires for Room Temperature Hydrogen Gas Sensors. *ACS Sens.* **2018**, *3*, 2152–2158. [CrossRef] [PubMed]
85. Li, Q.; Yang, S.; Lu, X.; Wang, T.; Zhang, X.; Fu, Y.; Qi, W. Controllable Fabrication of PdO-PdAu Ternary Hollow Shells: Synergistic Acceleration of H_2-Sensing Speed via Morphology Regulation and Electronic Structure Modulation. *Small* **2022**, *18*, 2106874. [CrossRef]